A seamless assessment of the role of convection in the water cycle of the West African Monsoon

C. E. Birch[1]*, D. J. Parker[1], J. H. Marsham[1], D. Copsey[2], L. Garcia-Carreras[1]

[1]Institute for Climate and Atmospheric Science, University of Leeds, Leeds, UK

[2]UK Met Office, Exeter, UK

*Now at UK Met Office, Leeds, UK

Corresponding author: C. E. Birch, Met Office, Leeds, UK (cathryn.birch@metoffice.gov.uk)

Abstract

A seamless suite of 40-day UK Met Office Unified Model simulations over West Africa during summer 2006 are analysed to investigate the causes of biases in the position of the rainbelt and to understand the role of convection in the regional water budget. The simulations include climate, global operational and limited-area runs (grid-spacings from 1.5 to 40km), including two 12-km runs, one with parameterised and one with explicit convection.

The most significant errors in the water-cycle terms occur in the simulations with parameterised convection, associated with the diurnal cycle and the location of the convection. Errors in the diurnal cycle increase the northward advection of moisture out of the Sahel towards the Sahara, but decrease the advection of moisture into the Sahel from further south, which limits the availability of moisture for Sahelian rainfall. These biases occur within the first 24 hours, showing that they originate from the representation of fast physical processes, specifically, the convection scheme. Once these rainfall regimes have been established, the terms of the water budgets act to reinforce the biases, effectively locking the rainbelt's latitude.

One of the simulations with parameterised convection does, however, produce a better latitudinal distribution of rainfall because on the first day it is better able to trigger convection in the Sahel. Accurate representation of the diurnal cycle of convection and the ability to trigger convection in a high convective inhibition environment is key to capturing the water cycle of the region and will improve the representation of the West African Monsoon.

1 Introduction

The accurate prediction of rainfall at weather and climate timescales is critical for both the prediction of hazardous weather (floods, drought) and for water and food security under climate change. These aspects are particular issues in West Africa, where society is generally more vulnerable to variability and change than elsewhere. Although significant advances have been made in the last decade, the West African Monsoon (WAM) is not well understood and difficult to predict on all scales. Some of the most significant issues include the position of the rainbelt [*Hourdin et al.,* 2010], north-south displacements in the mean atmospheric circulation patterns [*Tompkins,* 2005], the diurnal cycle [*Yang and Slingo,* 2001] and the surface fluxes [*Boone et al.,* 2009a]. Climate models are still unable to predict with any confidence whether precipitation will increase or decrease in the future [*Cook*, 2008; *Biasutti et al.,* 2009].

The Year of Tropical Convection Project (YOTC, *Waliser et al.,* 2012) recognised that it will be impossible to predict climate on regional scales, nor to comprehend the global water cycle, without addressing tropical convection and its multiscale organisation [*Moncrieff et al.,* 2012]. In reality, tropical convection peaks over the West African continent during the late afternoon, after the solar maximum, because convective circulations require time to overcome the convective inhibition and mid-level dryness [*Duvel,* 1989; *Nesbitt and Zipser*, 2003; *Dai,* 2007]. In some regions of West Africa there is a secondary peak in the early hours of the morning, caused by storms that form over the mountainous regions to the east and propagate westwards overnight [*Duvel,* 1989]. Models of all scales that parameterise convection do not produce these propagating systems, but instead produce rainfall that is too light and whose diurnal cycle peaks too early in the day [*Yang and Slingo*, 2001; *Dai,* 2006; *Guichard et al.,* 2010; *Stephans, 2010; Nikulin et al.,* 2012]. Models with finer horizontal grid-spacings that are able to allow convection to develop explicitly tend to have improved diurnal cycles [*Guichard et al.,* 2004], although the amount of rainfall is often overestimated [*Weissman et al*., 1997; *Holloway et al.,* 2012]. *Pohl and Douville* [2011] and *Dirmeyer et al.* [2012] both show that it is the change in the representation of the physical processes, rather than simply the increases in the horizontal grid-spacing that causes these improvements.

Recent work has made some progress towards improving convective parameterisation schemes. Embedding a cloud-resolving model into lower-resolution simulations can improve the diurnal cycle [*Dirmeyer et al.,* 2012] and representing the role of boundary-layer thermals [*Rio et al.,* 2009] and cold pools [*Grandpeix and LaFore,* 2010] in convective triggering shifts the diurnal peak in rainfall to late afternoon [*Sane et al.,* 2012]. Allowing

the entrainment rate over land to vary with the height of the lifting condensation level also improves the diurnal cycle of convection [*Stratton and Stirling,* 2012; *Stirling and Stratton*, 2012].

Marsham et al. [2013] used 10-day simulations from the Cascade project, with both explicit and parameterised moist convection at the same 12-km grid-spacing ("12kmExp" and "12kmParam"), as well as a simulation at 4-km grid-spacing, to demonstrate the impact of the representation of convection on the larger-scale circulation. Their findings are summarised in Figure 1a-d, in which all four panels show a south-north transect from the climatological near-surface high pressure in the Gulf of Guinea (south of 5°N) to the Saharan Heat Low (SHL) to the north. The majority of the moisture associated with the monsoon is advected at low levels over the continent from the Gulf of Guinea in the southwesterly winds that are forced by the north-south pressure gradient [*Duvel*, 1989]. In 12kmParam convection is triggered too early (~1200 UTC, Figure 1c), although the amount of triggering north of ~12°N at any time of day is very limited. The additional cloud cover means that the surface is not heated as much by shortwave radiation as in 12kmExp. During the daytime the synoptic flow in both models is inhibited by dry boundary-layer (BL) convection that produces significant mixing within the lower atmosphere (Figure 1a and c; *Parker et al.,* 2005). By 2100 UTC the more realistically timed moist convection in 12kmExp is active between the coast at 5°N and the Sahel at 17°N (Figure 1b). Solar heating from earlier in the day and moist convective heating (which dominates) warms the atmosphere in 12kmExp, which creates a relative low pressure at the surface in the Sahel (10-15°N). This weakens the flow from the Sahel to the Sahara, at the time in the diurnal cycle when boundary-layer convection has decayed and synoptic flows are most dominant. This is in contrast to 12kmParam, which has too strong a nocturnal flow between the Sahel and the Sahara (Figure 1d). *Marsham et al.* [2013] also show that cold pools form a major part of the monsoon in 12kmExp by transporting cool air and moisture northwards (Figure 1b), consistent with observations [*Garcia-Carreras et al.,* 2013]; these are essentially absent in 12kmParam.

A comprehensive study by *Meynadier et al*. [2010a,b] used a hybrid data set, including satellite observations, land-surface models and numerical weather prediction (NWP) analyses, to study the West African water cycle and evaluate model analyses and reanalyses. Some key biases in the water cycles of the model products were highlighted. Firstly, it is shown that the rain band is too far south in the models. In reality the Sahel is a net sink of water during the wet season (i.e. precipitation P > evapotranspiration E), but biases of 1-2 mm day^{-1} in the P and E rates mean that the Sahel is a moisture source in the models (i.e. P < E). Secondly, the hybrid data set

suggests that moisture flux convergence (MFC) occurs in the Sahel during the wet season but the models produce only very weak MFC, or even moisture flux divergence (MFD), in this region. The unrealistic MFD, coupled with a deep layer of dry air advected from the north at mid-levels, is thought to block the development of deep convection and the northward propagation of the monsoon rain band in the models. These conclusions are, however, were not examined at the process level by *Meynadier et al.* [2010b].

Much of the previous work on seamless prediction has focused on seasonal to climate scales (e.g. *Palmer et al.,* 2008; *Hurrell et al.,* 2009; *Hoskins*, 2013). Here we extend this framework to include scales ranging from climate and global NWP to convection-permitting simulations at 1.5-km horizontal grid-spacing. We expand on the work of *Marsham et al.* [2013] by extending the Cascade simulations from 10 to 40 days, including more comparisons with observations and by adding a climate simulation and limited-area simulations at 40 km horizontal grid-spacing with parameterised convection and at 1.5 km with explicit convection. The relative effects of biases in the diurnal cycle in moist convection and the location of moist convection were not separated in *Marsham et al.* [2013] but are in this study. The water cycle terms are also analysed in detail here. This is achieved through a model-process study with comparisons between the simulations with parameterised and explicit convection. None of the simulations are assumed to represent reality perfectly, but the differences between them inform our understanding of the processes that occur in reality.

Section 2 describes the model simulations, observational data sets and the methodology. Section 3 gives an overview of the biases in rainfall compared to the satellite-derived rainfall products. Section 4 links the biases in moist convection to the large-scale pressure gradients, winds and moisture advection and section 5 links model errors in the convection to the water budget and describes any feedbacks between the circulation and the water cycle. The results are then discussed and summarised in section 6.

2 Data and methods

2.1 Model simulations

All simulations are performed with the Met Office Unified Model (MetUM, *Walters et al.,* 2011). It has a semi-Lagrangian, semi-implicit and non-hydrostatic formulation and a terrain-following co-ordinate system [*Davies et al.,* 2005]. Parameterisations are used to represent unresolved aspects of the atmosphere, such as the surface [*Essery et al.,* 2001; *Best et al.,* 2011], the boundary layer [*Lock et al.,* 2000] convection [*Gregory and*

Rowntree, 1990] and mixed-phase cloud microphysics [*Wilson and Ballard*, 1999]. The capability of the model to perform simulations over a wide range of scales means it is ideal for a seamless study. A 10-year climate simulation, operational NWP analyses and a total of five simulations from the 'Cascade' project are used (Table 1).

The Cascade model configurations are Limited Area Model (LAM) MetUM runs, based on the high-resolution configurations developed by Lean et al. (2008) for use over the United Kingdom and are described in detail by *Pearson et al.* [2010; 2013]. Of the Cascade simulations, three were run with 'explicit' convection (horizontal grid-spacings of 1.5, 4 and 12 km) and two with 'parameterised' convection (horizontal grid-spacings of 12 and 40 km). The configurations of the Cascade models were designed to be as similar as possible except in the way they represent convection. The exception is 40kmParam, which was designed to have a configuration similar to the global operational version of the model. Radiation, boundary-layer mixing and convection are parameterised using the same schemes but some of the parameters and settings differ. In the 'explicit' simulations the closure time-scale of the parameterised convection is increased for high CAPE, leading to very little parameterised convection. *Pearson et al.* [2013] show that less than 1% of the rain is produced by the convection scheme, compared with more than 95% in the parameterised simulations.

The Cascade model configurations are run from 0000 UTC, 25 July 2006 for 40 days, until 0000 UTC 3 September 2006. This period was chosen to start after monsoon onset [*Janicot et al.,* 2008] and to coincide with one of the Intensive Observation Period of the African Monsoon Multi-disciplinary Analysis (AMMA) field campaign, for which many additional observations are available. The exception is the model with 1.5 km grid-spacing, which due to computing limitations, was run for only 9 days between 0000 UTC, 25 June 2006 and 0000 UTC, 2 August 2006. The simulations were initialised with European Centre for Medium-Range Forecasts (ECMWF) analyses and then forced only at the boundaries by either the ECMWF analyses or a set of lateral boundary conditions produced by the next-largest nest (see Table 1 for more details). The limits of the domains are illustrated in Figure 2.

Operational MetUM analyses from 25 June to 3 September 2006 are also included in the comparisons. The analyses are produced four times per day at 0000, 0600, 1200 and 1800 UTC and the t+3 hour forecast is added to this to produce a three-hourly dataset. For simplicity this data set is referred to as 'NWP'. The

operational version of the MetUM uses the same parameterisation schemes as described above, although many updates to the model have been made between this version that was operational in 2006 and the version that was used for Cascade.

The 10-year climate simulation is an atmosphere (and land) only simulation with prescribed daily sea surface temperatures and sea ice from *Reynolds et al*. [2007]. It has a horizontal grid spacing of 1.875° by 1.25° (195 km by 139 km at 20°N) and 85 vertical levels. Climatological averages were generated for each hour of the day for the month of August so that the climatological diurnal cycle can be analysed.

2.2 Observations and land-surface products

Satellite-derived rainfall products are used to evaluate precipitation in the model simulations. There is large uncertainty both in the amount and location of rainfall in these products, especially when high temporal and spatial resolution is required [*Roca et al.,* 2010; *Jobard et al.,* 2011]. Different products perform better over different regions within a continent and it is uncertain which product is the best to use over West Africa. For this reason the mean, maximum and minimum of four satellite products with temporal resolutions of between 30 minutes and 3 hours are used in the analysis.

The first data set is the Tropical Rainfall Measuring Mission product, TRMM-3B42 [*Huffman et al.,* 2007], which combines precipitation estimates from multiple satellites and land surface precipitation from rain gauges. The data is 3-hourly and the horizontal resolution is 0.25°. The CMORPH (CPC MORPHing technique, *Joyce et al.,* 2004) data set is another product with the same temporal and spatial resolution. It also uses precipitation estimates from multiple satellite radiometer (microwave) observations. Infra-red imagery is then used to propagate precipitation features during periods when the radiometer data are not available.

The Global Satellite Mapping of Precipitation product, GSMaP-MVK [*Ushio et al.,* 2009] uses a similar algorithm to CMORPH except it uses a different technique to refine rainfall with the infra-red imagery. The temporal and spatial resolutions are also higher, at 1-hourly and 0.1° in the horizontal. The Estimation of Precipitation by Satellites-Second Generation (EPSAT-SG) method was developed at Laboratoire de Météorologie Dynamique as a direct contribution to AMMA [*Bergès et al*. 2010]. It combines rainfall probability from the SEVIRI imager on the MSG (METEOSAT – Second Generation) satellite and information from TRMM with a rainfall potential intensity data set, derived by downscaling the Global Precipitation Climatology Project (GPCP)-1dd product.

The EPSAT-SG product is available every 30 minutes, at 0.1° horizontal resolution and within the region 5°S to 20°N and 25°W to 25°E..

The frequency and success of radiosonde observations in West Africa were increased significantly during the AMMA field campaign [*Parker et al.,* 2008]. A number of stations released 8 sondes per day during the Intensive Observation Periods (20-29 June and 1-15 August 2006). Unfortunately the humidity observations from some of the sondes released during AMMA suffered from a significant dry bias [*Bock et al.,* 2007], similar to that experienced in previous campaigns (e.g. during TOGA COARE, *Cieselski et al.,* 2003). Efforts have been made to reduce this (e.g. *Nuret et al.,* 2008), however comparisons between specific humidity from the model simulations and from the corrected observations in the lowest 1 km of the atmosphere show differences of at least a factor of two (not shown). In this study we are interested in evaluating the moisture flux, which is defined at the meridional wind, v, multiplied by the specific humidity, q, rather than the absolute humidity. Due to this, and the fact that the meridional wind dominates the variations in the $v*q$ signal in the model simulations, the observed humidity is not used in this study and instead, the observed wind vectors are compared directly to model winds.

The evapotranspiration product used in this study is from the AMMA Land-Surface Model Intercomparison Study (ALMIP) simulations (Boone et al., 2009b). A total of 11 different land-surface models, including the Joint UK Land Environment Simulator (JULES) that is used in the MetUM, were run for the period 2005-2007, at 0.5° horizontal resolution over the domain 17.5°W to 30°E and 5°S to 20°N. The models were forced with near-surface temperature, humidity, wind and pressure data from ECMWF operational forecasts, radiative fluxes from the Land Surface Analysis Satellite Application Facility (LSA SAF, *Geiger et al.,* 2008) and rainfall from TRMM-2B42. Land surface parameters, such as albedo, vegetation cover fraction, soil texture, were taken from the Ecoclimap database [*Masson et al.,* 2003]. Model diagnostics, including surface evapotranspiration were saved every 3 hours.

2.3 Method

The methodology followed here is similar to that employed by *Meynadier et al.* [2010a; 2010b]; the amount of precipitable water in each atmospheric column in the model can only change through exchange with the

surface by evaporation and precipitation, or through horizontal advection. The vertically integrated atmospheric water budget equation is expressed as [*Peixoto and Oort,* 1983]:

$$\frac{\delta}{\delta t}\frac{1}{g}\int q dp = E - P - \nabla.\frac{1}{g}\int qV dp, \qquad (1)$$

where *E* is the evapotranspiration from the surface, *P* is the precipitation at the surface, *q* is the specific humidity in the atmosphere at height *z* and *V* is the horizontal wind velocity vector at height *z*. The vertical integrals are computed from the surface to the uppermost atmospheric model level. The term on the left-hand side represents the precipitable water vapour tendency (PWVt) and the third term represents the moisture flux divergence (MFD). Equation (1) can be rewritten as:

$$PWVt = E - P - MFD. \qquad (2)$$

All four terms are computed from diagnostics produced by the limited area simulations, whilst only *E* and *P* are available from the NWP analyses and the climate model simulation. Satellite products are used for estimates of observed *P* and an ensemble of land-surface models are used to get an estimate of *E*.

One of the key comparisons is between the two 12-km simulations with explicit and parameterised convection. These simulations are identical apart from their representation of convection. Neither simulation can be viewed as a true representation of reality; 12 km is coarse for the explicit representation of convection, although it can give reasonable squall lines, which are the dominant mechanism for rainfall in the Sahel [*Weisman,* 1997; *Mathon et al.,* 2002], and the configuration with parameterised convection suffers from many of the biases common in lower resolution models. Understanding is gained from comparing the two 12-km configurations and then the differences can be related back to both the higher-resolution (4kmExp and 1.5kmExp) and the lower-resolution (40kmParam, analyses and climate) configurations.

3 Rainfall biases

The mean diurnal cycle of rainfall for the observations and each of the model configurations is shown in Figure 3. Data are analysed between 8°W-6°E and 7.5-24°N, marked by the grey box in Figure 2. This domain was chosen to avoid any signal in the rainfall from coastal regions and to remove the very high rainfall rates that occur over the Guinea highlands to the west and the various mountain ranges to the east. The primary peak in rainfall in the observations occurs at 1800 UTC, which is due to the daily diurnal peak in locally-produced

convection. Convection is also triggered daily over the mountainous regions to the east of the analysis domain. These systems become organised and propagate westwards. They reach the analysis domain in the early hours of the morning, which explains the secondary peak in the observations at 0400 UTC. Differences of 3-4 mm day^{-1} between the satellite products with the lowest and highest estimates (grey zone in Figure 3) justify the need for the use of four different data sources for comparison with the model simulations.

The models that parameterise convection (solid lines) all peak between 1200 and 1400 UTC, which is too early compared to the observations. This is a common issue within models [*Yang and Slingo.* 2001] and is in agreement with previous studies that use the MetUM (e.g. Lean et al., 2008). The majority of the rain in these simulations is produced by localised storms, i.e. unlike reality very few long-lasting propagating systems are formed. 4kmExp and 1.5kmExp peak at 1800 UTC in agreement with the observations. 12kmExp peaks approximately 3 hours too late due to the relatively coarse grid spacing [*Weisman et al.,* 1997]. All three of the explicit models overestimate the total amount of rainfall, which almost completely masks the early-morning signal from the propagating systems, even though they do exist in these simulations (not shown, see *Pearson et al.,* 2013).

Figure 4 shows the mean rainfall amounts by latitude between 8°W and 6°E. The observed rainfall peaks at 12°N, with an uncertainty in the absolute amount of approximately 6 mm day^{-1}. Model maxima vary by almost a factor of three and in general the configurations with parameterised convection peak further south than the configurations with explicit convection. There is a stark contrast between the two simulations with 12 km grid-spacing; 12kmParam peaks at 8°N and 12kmExp peaks at ~13°N.

A comparison of the mean rainfall by latitude produced by 12kmParam and 40kmParam also highlights some interesting differences. The peak in rainfall in 40kmParam is at least 4° further north and the amount of rainfall in 40kmParam is much greater compared to that in 12kmParam. Differences in the formulation of the parameterisation schemes, possibly combined with the difference in grid-spacing, means 40kmParam is able to trigger much more convection north of 12°N and produces greater precipitation rates compared to 12kmParam.

4 Effect of moist convective biases on the large-scale circulation

4.1 Meridional pressure gradients and moisture fluxes

Figure 5a shows the mean diurnal cycle of the difference in 925-hPa geopotential height between the Sahel and the Sahara (15 to 20°N). Overall 12kmParam has a larger Sahel-Sahara pressure gradient than 12kmExp because both convective and solar heating is weaker in the Sahel in 12kmParam, which increases the near-surface pressure (compare Figure 1b and 1d). In 12kmParam the geopotential height difference between 15 and 20°N is greatest at ~2100 UTC after the main period of moist convection and is smallest at ~1500 UTC (Figure 5a), shortly after the maximum in convective heating. 40kmParam has almost the exactly the same diurnal cycle as 12kmParam. The maxima and minima in the other two configurations with parameterised convection (climate and analyses) are also at approximately 2100 and 1200 UTC respectively, although their absolute differences are lower. In the case of the NWP analyses this is most likely due to the assimilation of observations every 6 hours, which bring the model values closer to reality (e.g. *Garcia-Carreras et al.* 2013). In the climate model the entire monsoon system is positioned too far south (see Figure 6b), a common issue in climate simulations [*Nikulin et al.,* 2012], which causes the absolute difference to be lower than in the other parameterised model configurations. The three configurations with explicit convection all have a relatively low mean difference, consistent with *Marsham et al.* [2013] and the schematic in Figure 1b, and the diurnal cycle is much weaker due to the evening maximum in rainfall and since the rainfall is distributed more evenly over the day (Figure 3). The difference is lower in 1.5kmExp than in 4kmExp and 12kmExp, which may be related to the differences in rainfall amounts between 13 and 16°N (Figure 4).

The parameterised and explicit model configurations also exhibit contrasting behaviour to the south of the Sahel. First we compare the 925-hPa geopotential height difference between the coast and the south Sahel (5 to 10°N) in 12kmParam and 12kmExp (Figure 5b). The pressure gradient in 12kmParam is at a maximum at 1200 UTC, at the peak of the moist convection and is at a minimum at ~2200 UTC, after the convection and therefore when the relative high over the Sahel is at its strongest (Figure 1d). 12kmExp has a larger coast-Sahel pressure gradient overall and it peaks at ~2100 UTC, when the convective heating is at its maximum (Figure 1b). The pressure gradient in 40kmParam, the climate configuration and the NWP analyses peaks at ~1200 UTC, similar to 12kmParam. Note that the mean gradient over the day is larger in 40kmParam than in 12kmParam (discussed later in section 6). The pressure gradients in 4kmExp and 1.5kmExp peak at a similar time to 12kmExp.

Differences in the pressure gradient cause differences in the low-level circulation, especially at night, when turbulent mixing is at a minimum. Figure 6b-h shows the mean diurnal cycle in the moisture flux (meridional wind, *v*, multiplied by the specific humidity, *q*) at 400 m above ground level (agl), averaged between 8°W and 6°E for each of the models. The variations in the magnitude of the flux in all model configurations are dominated by *v* (not shown). The limited northward extent of the monsoon in the climate simulation is also apparent in this figure. All the models exhibit a similar basic diurnal cycle, where the monsoon flow from the south is inhibited during the day by boundary-layer convection and accelerates at night, transporting water towards the SHL at low levels [*Parker et al.,* 2005]. Between 15 and 20°N this low-level nocturnal transport is stronger in the climate simulation, 40kmParam and 12kmParam compared to the NWP configuration and the three explicit simulations because the meridional pressure gradients are different (Figures 5 and 1). The NWP analyses used here are constrained by observations, which explains why the moisture flux is smaller than in the other simulations with parameterised convection.

The moisture flux south of 13°N also varies significantly between the parameterised and explicit model configurations. All the configurations with parameterised convection have a peak in $v*q$ at 5°N at around 1500 UTC that moves to 10°N by 0600 UTC. Immediately to the north of this (10-13°N) the northward nocturnal flux is significantly larger in 40kmParam than 12kmParam. This is an important difference between the two configurations with parameterised convection and is discussed in more detail in section 6. The moisture flux south of 10°N in the explicit simulations is generally larger than that from the parameterised simulations and the peak is later (1800-0000 UTC), coinciding with the later peak in pressure gradient in the explicit simulations in Figure 5b.

Figure 6a compares the mean meridional moisture flux by latitude from each of the model configurations. The peak in the northward moisture flux in 40kmParam and 12kmParam is well illustrated between 14 and 18°N. This peak also occurs in the climate simulation, although it is further south due to the displacement of the entire monsoon system. The explicit simulations produce a much lower moisture flux at these latitudes. To the south the difference between the parameterised and explicit model configurations is much smaller since the differences between them tend to average out over the diurnal cycle.

4.2 Evaluation of meridional fluxes using radiosonde data

The differences in the large-scale moisture advection shown in Figure 5 can be evaluated with radiosonde observations from four different stations. The stations of Agadez (17.0°N, 8.0°E), Niamey (13.5°N, 2.1°E), Tamale (9.4°N, 0.8°W) and Cotonou (6.5°N, 2.5°E) are used because these stations form an approximate north-south transect across the West African continent and because 3-hourly sondes were launched over a two-week period in August 2006. The plot for Parakou (9.4°N, 2.6°E, not shown) is very similar to that at Tamale, which is at a similar latitude. The latitudes of the radiosonde stations are marked on the panels of Figure 6 by the horizontal white lines. The model diagnostics are taken from the location of the radiosonde station except for the climate model diagnostics at Agadez, which are taken from 14°N to account for the incorrect position of the monsoon system. Figure 7 shows the comparisons between the observations and the simulations. Agadez is located at almost exactly the same latitude as the peak in v^*q in the 12kmParam and 40kmParam simulations (17°N, Figure 6). The observations show that the meridional wind is mainly northerly at this latitude, apart from in the early hours of the morning, when it is southerly (Figure 7a). The magnitude of the mean wind when it is southerly does not exceed 1 ms^{-1}. The diurnal cycle in v in the explicit configurations all collapse onto approximately the same curve and the magnitude and direction is similar to that observed, although12kmExp peaks too early. In contrast, the nocturnal flow between the Sahel and the Sahara in the parameterised simulations is far too strong and is maximised around 0000 UTC.

At Niamey the observed meridional wind varies by approximately 2 ms^{-1} through the diurnal cycle, with the peak at ~0000 UTC (Figure 7b). 12kmExp and the NWP analyses match the observations best. Again, the parameterised model configurations produce a too strong nocturnal flow from the Sahel towards the Sahara. 4kmExp and 1.5kmExp have rather too light winds with a diurnal cycle delayed by around 3 hours. At Tamale the observed flow is southerly and peaks overnight and during the morning. The simulations also all peak overnight (Fig 7c), with minima around 1800 UTC, but apart from that the picture is less clear. At Cotonou all configurations give a reasonable timing of the 0900 UTC minimum and 0000 UTC maximum, but the explicit models produce too strong a peak in southerly winds (Figure 7d). It is not clear why this is the case. The excessive southerly winds in explicit models could be because the near-surface pressure in the Sahel in the explicit simulations is too low due to the large precipitation rates (Figure 3), which would increase the pressure gradient between the coast and the Sahel and thus increase the meridional wind. Alternatively it could be because the explicit configurations over-predict the strength of the sea breeze, although occurrences of the

sea breeze are less common during the wet season compared with other times of year [*Bajamgnigni Gbambie and Steyn,* 2012]. The radiosonde location at Cotonou is also situated on the south side of an inland lagoon, which could also affect local wind conditions.

5 Water budget

5.1 Evapotranspiration and precipitation

Having shown the impact of convective parameterisations on the monsoon circulation, we now consider the impacts these differences have on the regional-scale water budget, as described in Equations 1 and 2. Figure 8 shows the mean evapotranspiration by latitude for each of the model configurations, the range and mean of the ALMIP land-surface model simulations (grey area and black solid line) and a separate line representing the mean of the JULES model from the ALMIP simulations (the surface scheme used in the MetUM, black dashed line).

Compared to the ALMIP multi-model mean, all the model configurations overestimate the evapotranspiration rate, which is unsurprising given that they also overestimate the amount of rainfall (Figure 4). The two configurations with 12 km grid-spacing produce values of evapotranspiration closest to that from the ALMIP models and these are also the models with the lowest rainfall rates. The range of the ALMIP models is approximately 2 mm day^{-1}, and the peak values occur at latitudes between 11 and 15°N. The peak in the climate simulation is much further south than in the ALMIP multi-model mean and in other model configurations because the entire monsoon system is further south (Figure 6). The peak in all of the other model configurations is between approximately 13 and 15°N, which is generally further north than their peak in precipitation. This could be because the warmer temperatures and clearer skies in the north allow greater evaporation than within the main rainbelt or it could be due to the way the soil moisture was initialised: the Cascade simulations were initialised with a climatological soil moisture distribution. The variability of the top layer of soil appears to spin up within a couple of days (Chris Taylor, personal communication), but the lower layers require a spin-up time of more than a month (not shown), which was not possible for these simulations. This limitation should be considered during the analysis of the water budget terms in the remainder of this section.

Figure 9 shows maps of 40-day mean evapotranspiration minus precipitation, *E-P*. The satellite and model-derived product (TRMM minus ALMIP, called 'observations' here for simplicity) suggest that *E-P* is negative across the entire continent up to ~17°N, apart from a small region near the coast between 10°W and 0°W (Figure 9a). This is expected, since the 40-day mean represents the middle of the wet season, in which the surface should getting wetter. The region of positive E-P values to the south occurs because the main monsoon rains have already passed over this region and the rainbelt now resides further north, limiting the rainfall near the coast and allowing rain that has previously fallen to evaporate from the surface. The values remain large and negative to the east of this (2 to 10°E) because a significant amount of convection is initiated over the Cameroon highlands (3-7°N, 9-17°E), which propagates westwards.

The model configurations with explicitly-resolved convection produce negative values of *E-P* in a similar location to those observed as well as the region of positive values to the south (Figure 9f-h). The negative values are however, too large in magnitude because the explicit simulations produce too much rainfall (Figure 4). 1.5kmExp has large positive values to the east of the domain that occur because very little rain has fallen in this region in the 9-day simulation and thus the soil moisture with which the model was initialised evaporates over the course of the simulation.

The climate simulation reproduces the general spatial patterns of *E-P* but the entire monsoon system is too far south, causing *E-P* to be zero or slightly positive in the Sahel region (Figure 9b). There was an error in the soil moisture scheme in the NWP version of the model that was operational in 2006 that caused significant drying in the east of Africa (Sean Milton, personal communication), which is apparent east of 10°E in Figure 9c. Further west the *E-P* pattern looks more similar to the observations, except for a region of drying soil at 15°N. 12kmParam is the worst-performing configuration (Figure 9e); the negative values of *E-P* only extend to 13°N and north of this there are strong positive values between 13 and 17°N. Evapotranspiration rates that exceed the precipitation rate are totally unrealistic for this time of year (as noted for the ECMWF model by *Meynadier et al.,* 2010a). The positive values are explained by the low precipitation rates in the Sahel in 12kmParam and by the evaporation of the soil moisture with which it was initialised. *E-P* in 40kmParam is more reasonable compared to the observations because more rain falls in the Sahel region in this simulation (Figure 9d). The large differences between the representation of the water budget in 12kmParam and 40kmParam are important and are discussed further in the following sections.

5.2 Moisture flux divergence

The 40-day mean MFD for each of the Cascade model configurations is shown in Figure 10b-f and the mean by latitude is shown in Figure 10a. Positive values represent a loss of water from the atmospheric column (MFD) and negative values represent a gain of water in the column (MFC). All the configurations apart from 12kmParam display significant MFC between 8 and 15°N, which coincides with the region of maximum rainfall in each simulation. On average 12kmParam produces MFD between 13 and 15°N; here rain is supported by evaporation rather than MFC, consistent with the surface drying there (Figure 9). 12kmExp, 4kmExp and 40kmParam produce MFD to the south of 8°N, consistent with the lack of rainfall in this region. In contrast, 12kmParam and 1.5kmExp produce MFC near the coast (5-9°N), consistent with the more southerly position of their rainbelts (Figure 4),

Figure 11 shows the mean diurnal cycle of MFD, *P* and *E* for each of the Cascade model configurations. In 40kmParam and 12kmParam the timing of *P* and *E* coincide because the rainfall peaks at the solar maximum when *E* is at its highest. In 12kmParam the latitudinal peak in *E* is further north than the peak in *P*, which illustrates the *E-P* bias caused by the soil moisture initialisation that is highlighted in Fig. 9. MFC (blue shading) occurs during the day between the coast and the northerly extent of the rainfall in the parameterised configurations. Overnight the moisture advection becomes divergent (red shading) north of 12°N due to the strong northward nocturnal moisture flux illustrated in Fig. 6. The nocturnal divergence of moisture from the region 12-17°N reduces the ability of the model to produce rainfall in this region the following day, which appears to contribute to 'locking' the rainbelt in its southerly position.

The explicit configurations show a substantially different mean diurnal cycle, driven by the fact that *E* is out of phase from *P*. As a result, the atmosphere is moistened by the combination of evaporation and MFC over the entire diurnal cycle; *E* adds moisture during the day, when MFC is weak but mainly positive, while MFC adds moisture overnight during the period of peak rainfall. This constant supply of water, especially in the northern Sahel, maintains a good source of moisture the following day for further rainfall. We can infer that the maintenance of atmospheric moisture by *E* and MFC throughout the diurnal cycle, in the explicit models in the zone 12-17°N, allows the rainbelt to exist in a more northward location than in the model configurations with parameterised convection.

5.3 Total budget

All components of the water budget are now examined in parallel for each of the Cascade model configurations. For each of the three sub-regions illustrated by the grey boxes in Figure 2, daily means of each of the terms are computed and then the cumulative sum of each of the terms is plotted (Figures 12-14). The total column integrated MFC is plotted (solid red line), as well as the integrated MFC in the monsoon layer (0 - 2000 m agl, dashed red line) and the integrated MFC at mid-levels (2880 - 4500 m agl, dotted red line). The precipitation term (green line) is multiplied by -1 so that the positive side of the y-axis represents the components that add moisture to the atmosphere and the negative side of the y-axis represents the components that remove moisture from the atmosphere. Note that observations are not available for the computation of MFC and the 1.5 km simulation was only run for 9 days.

Figure 12a shows the observed water budget components for the northern-most analysis box. Over the course of the 40 days, 50 mm of rain was observed to fall in this region and almost all of this was evaporated back into the atmosphere (E-$P \approx 0$), which is expected in the hot, arid environment of the northern Sahel. 4kmExp overestimates the total amount of precipitation by approximately 20 mm over the 40 days (Figure 12e), which means the magnitude of E-P is 20 mm, rather than zero as suggested by the observations (the heavy rain rates in 4kmExp result in rain lost as run-off, which is not available for re-evaporation). 40kmParam, 12kmParam and 12kmExp slightly underestimate the amount of precipitation and the amount of evapotranspiration is also small compared with the observations, resulting in near zero values of E-P over the 40 days, similar to that observed. The accumulated total column MFC (red solid lines) from the model configurations is positive over 40 days, i.e. moisture is on average transported into this region. Moisture is advected into the region within the monsoon layer (red dashed lines) and advected out of the region at mid-levels (red dotted lines), consistent with moisture transported from the monsoon layer to mid-levels by dry and moist convection. The total MFC is the difference of two larger terms, which shows the importance of accurate modelling of vertical transport for the water budget. The precipitable water vapour tendency (PWVt) is variable but generally positive over the 40-day period, indicating that the total amount of atmospheric water increases over the 40-day period in the region 17.5-24°N.

Figure 13 shows the same cumulative water budget plots for the southern box illustrated in Figure 2. Unlike the northern box, in this region the observed *E-P* is negative, i.e. it rains more than it evaporates over the 40-day period, which is expected during the wet season. Also in contrast to the northern box, in all model configurations the MFC approximately balances *E-P* so that the total amount of water in the atmosphere stays almost constant over the 40 days (i.e. PWVt ≈ 0 in all models). This is in agreement with *Meynadier et al.,* [2010a] who state that PWVt exhibits low variability compared to the other terms because in the middle of the wet season the relative humidity values are close to saturation. 40kmParam, 12kmExp and 4kmExp all overestimate the amount of rainfall and although the high evapotranspiration rates partly compensate, the *E-P* values are too large in magnitude. The rainfall rates in 12kmParam are more similar to the observations but *E* is overestimated, leading to magnitudes of *E-P* that are too small. The vast majority of the advection occurs within the low-level monsoon flow (compare solid/dashed/dotted red lines). This is in agreement with *Bielli and Roca* [2009] and *Meynadier et al.* [2010a] who show that there is a strong correlation between precipitation and MFC in the monsoon layer.

The water budgets for the mid-box (12.5-17.5°N) are shown in Figure 14. For the observations and all the model configurations except 12kmParam, the behaviour of P and E are similar to those in the southern box; i.e. *E-P* is negative (surface wetting), although the simulations overestimate the precipitation rate. Like the southern box, the total column water is approximately constant, consistent with this mature phase of the WAM. 12kmParam is however in disagreement with the other models; it does not rain enough in this region and thus *E-P* is positive, i.e. the surface is moistening the atmosphere and MFD occurs (i.e. moisture is advected out of the region), which is inconsistent with all the other model configurations and observations.

The progression of the cumulative terms over the course of the 40 days in the mid-box also contains some information about the difference between 12kmParam and the other model configurations. Note that the terms of the water budget are similar in all the model configurations until day 10, even though the meridional circulation and diurnal cycle biases appear from the first day. Prior to this day, in 12kmExp the gradient of the precipitation line is small (low rainfall amounts) and then steepens between day 10 and 14 (high rainfall amounts). This high rainfall event is associated with the first significant African Easterly Wave (AEW) in the simulation, which brings significant westward-propagating convection and rainfall to the Sahel (not shown). In 12kmExp and 4kmExp this generates a sudden increase in rainfall and MFC and a northward shift in the

convection (note that the AEW events are not reproduced in 1.5kmExp because the simulation was only 9 days long). Further significant AEW events occur in the explicit simulations on day 27 and 35, which produce a similar response in the water budget, and with the largest AEW event on day 35 also affecting the water budget in the parameterised runs. The water budget terms in the two model configurations with parameterised convection progress differently through the 40 days. In both 40kmParam and 12kmParam the rainfall is more constant over the 40 days and no significant propagating AEW rainfall events occur apart from one associated with the largest AEW event on day 35. The AEW events appear in the east of the domain (due to the lateral boundary conditions) and the waves propagate westwards, although they are weak and little rainfall is associated with them (not shown). The reasons for this are unclear and are beyond the scope of this paper, although a follow-up study focusing on convection-synoptic couplings and changes in the water budget on shorter timescales is planned for the near future.

6 Discussion and conclusions

This study uses a seamless suite of model simulations to examine the role of moist convection in the water cycle of the West African Monsoon (WAM). Large-domain limited area model simulations with various grid-spacings were performed over a 40-day period during summer 2006 as part of the Cascade project. Simulations were run with parameterised convection at 40 and 12 km, with explicit convection at 12, 4 and 1.5 km and were compared to NWP analyses and a 10-year climate simulation.

The analysis highlights some fundamental differences in the way the WAM is represented in the various simulations. Compared to 40kmParam and 12kmParam, the simulations with explicit convection rain more in the north (i.e. in the Sahel) and the rainfall occurs later in the day. The reduced convection during the day in the explicit simulations leads to increased heating in the Sahel by shortwave radiation. This coupled with greater nocturnal convective heating creates a low pressure at the surface, which decreases the mean pressure gradient between the Sahel and the Sahara, particularly at night when there is no boundary-layer convection and synoptic flow is maximised. The southerly winds between the Sahel and the Sahara are therefore weaker in the explicit simulations than the simulations with parameterised convection (Figure 1b,d,f), which is in agreement with the findings of *Marsham et al.* [2013]. This study shows that the conclusion

holds for a larger range of models with different resolutions and we extend the analysis by considering the effect on the pressure gradients further south and the overall effect on the water budget.

The relative low pressure in the Sahel in the explicit simulations acts to increase the pressure gradient between the Guinea coast and the Sahel, again most significantly at night, increasing the southerly winds in this region (Figure 1b,d). The meridional circulation has a significant effect on the advection of moisture into and out of the Sahel. Due to the large pressure gradient, the moisture flux from the Sahel into the Sahara is too large in the parameterised simulations (Figure 6 and 11). In addition, the small pressure gradient between the coast and the Sahel in 12kmParam produces a moisture flux into the Sahel which is weak. This dries the Sahel in 12kmParam because the moisture advected towards the Sahara is not replaced from the south (blue blocks, Figure 1d). In contrast, in the explicit simulations the Sahel-Sahara moisture flux is weaker and the coast-Sahel flux is stronger, allowing a sufficient amount of moisture to be available for convection in the Sahel (blue blocks, Figure 1b). This difference is reflected in the MFC in Figure 14c and d, which show net advection into the Sahel in 12kmExp (MFC) but net advection out of the Sahel (MFD) in 12kmParam, with rain being sourced from soil moisture that unrealistically dries through the simulation.

The 12kmParam and 12kmExp runs differ only in their representation of convection. Figure S3 in the supplementary material of *Marsham et al.* [2013] shows that their differences in both moist convection and circulation develop on the first afternoon of the 40-day simulations. The differences in circulation and the associated moisture advection in the 12km runs must therefore originate from differences in the representation of moist convection. Once the low-level pressure and circulation biases in the parameterised simulations are established on day 1, they are able to feedback and reinforce the biases in the convection. The lack of rainfall in the Sahel in 12kmParam produces a positive feedback; it acts to reduce MFC in the Sahel and so prevent further rain, effectively 'locking' the rainbelt in place. In the explicit simulations the convection occurs at night, when turbulence is at a minimum and the meridional flow is at its strongest. The relatively weak Sahel-Sahara pressure gradient results in less northwards moisture transport out of the Sahel, in agreement with observations. Further south the pressure gradient is relatively strong, which produces stronger winds and an increased moisture flux towards the Sahel, making more moisture available for further rain.

A second major difference between the explicit and parameterised simulations is the way the rainfall is coupled to AEWs. All the Cascade simulations are forced by ECMWF analyses at the model boundaries, which means that AEWs arrive at the eastern boundary at the same time in all the simulations. In the explicit simulations significant rainfall is associated with the westward propagation of these waves, whereas in the parameterised simulations the waves are much weaker and have little rain associated with them. The first major AEW event occurs on day 10 in the simulations, which provides a 'kick' to push the rainbelt northwards in the explicit simulations. The parameterised models are unable to sustain a rainfall-response to this forcing and thus it is on this day that the Sahelian water budgets in the parameterised and explicit simulations begin to significantly diverge (Figure 14).

40kmParam provides an interesting and contrasting case to 12kmParam. The configurations of 40kmParam and 12kmParam are differ slightly and so any differences between the two simulations must be related to this or the difference in grid-spacing. Both configurations suffer from the same issues with the diurnal cycle (Figure 1e,f): like 12kmParam, 40kmParam rains too early in the day, which causes a too strong pressure gradient between the Sahel and the Sahara and as a consequence there is a too strong northward nocturnal moisture flux out of the Sahel. The important difference is, however, that 40kmParam is able to trigger more convection in the Sahel (Figure 1e), which means the pressure gradient between the Gulf of Guinea and the Sahel is stronger in 40kmParam than in 12kmParam (Figure 5b) and thus the moisture flux into the Sahel is larger (Figure 6a, compare blue and red solid lines 7-15°N). This is summarised by the blue blocks in Figure 1f; the greater amount of moisture advection replaces that lost to the Sahara and thus allows further precipitation. This explains why the water budget in 40kmParam is better than in 12kmParam in the Sahel, despite its excessive Sahel-Sahara flow

The NWP analyses display the same biases in the diurnal cycle of rainfall as the other parameterised simulations. The effect on the pressure gradients and circulation is however less significant because to some extent the observations that were assimilated to create the analyses correct the circulation, although significant errors remain, especially in the Sahel.

The climate simulation displays the same biases in the diurnal cycle of convection as the other parameterised configurations. This produces similar errors in the diurnal cycle of the pressure gradients and a too strong

northward moisture flux, similar to the other parameterised configurations. In contrast to the limited area model simulations with parameterised convection, the northward extent of the monsoon flow in the climate configuration is approximately 500 km further south. As well as having a much larger grid-spacing, the climate simulation is free-running and is not forced at the boundaries by analyses as are the Cascade limited-area simulations. Biases in the large-scale transport into the region, through phenomena such as AEW's, and larger-scale processes such as teleconnections are likely to be reasons for this difference.

Some of the biases found in the 12kmParam simulation are similar to those found in the reanalysis products evaluated by *Meynadier et al.* [2010b]. Firstly, the ECMWF Re-Analysis (ERA)-Interim and the National Centers for Environmental Prediction (NCEP) Reanalyses I and II all produce positive E-P values in the Sahel in contrast to the observations, a similar bias to that produced by 12kmParam. Secondly, in the Sahel both the reanalysis products and 12kmParam produce MFD or only very weak MFC, instead of larger values of MFC as suggested by the explicit models in this study and by the hybrid data set in *Meynadier et al.* [2010b]. The similarities between 12kmParam and the reanalysis products reinforce the conclusion the model biases are due to the incorrect representation of physical mechanisms and thus the results from this study are applicable not just to the MetUM, but to other models with various horizontal resolutions that employ a convective parameterisation.

The explicit configurations are not without errors and should not be viewed as a representation of 'truth'. They are a different (as compared to the parameterised configurations) realisation of reality but with an improved ability to represent the diurnal cycle and propagating convective systems. From day 1 onwards the explicit configurations significantly overestimate the amount of rainfall and once these biases in the amount of rainfall form, they are able to feedback on other aspects of the water cycle. Much of the surplus rainfall is compensated for by large evapotranspiration rates (Figure 8), although *E-P* remains too large in magnitude compared to the observations. This increases the moisture transport (MFD) in the southern regions to values that are likely larger then those observed (e.g. Figure 13b and e). The strong southerly winds in the explicit simulations in the south of the continent (Figure 7c, d) may also be a result of too much rain and convective heating further north, which creates a positive bias in the coast-Sahel pressure gradient and in the associated northward transportation of moisture.

The simulations used in this study differ only in their representation of convection, so the significant improvements in the explicit configurations must be due to their ability to represent convection more accurately. This suggests that many of the issues in representing the WAM are likely due to the representation of convection rather than other factors such as vegetation, cloud microphysics or the production of AEW to the east. A good representation of the diurnal cycle and location of convection are key for an accurate representation of the monsoon because once the location is determined by the convection scheme, feedbacks reinforce any biases, locking the rainfall in position. The ability of a parameterised model to trigger deep convection in the Sahel (i.e. in a high CIN environment) appears to be of the upmost importance for maintaining rainfall there, although this does not solve errors in transport resulting from errors in the timing of the convection, or from lack of cold pools [*Marsham et al*., 2013; *Garcia-Carreras et al.,* 2013]. A planned extension to this study is to investigate the response of convection to the AEW's forced at the east boundary in the different model configurations and to determine how the water budget responds to these events on shorter timescales (< 1-2 days).

Acknowledgements

CB produced this work as part of the AMMA-II project, which was funded by Natural Environmental Research Council (NERC) grant NE/G018499/1. The model simulations were performed by Grenville Lister at NCAS-CMS (National Centre of Atmospheric Science – Computer Modelling Support) as part of the *Cascade* project, which was funded by Natural Environmental Research Council grant NE/E003826/1. This work made use of the facilities of HECToR, the UK's national high-performance computing service, which is provided by UoE HPCx Ltd at the University of Edinburgh, Cray Inc and NAG Ltd, and funded by the Office of Science and Technology through EPSRC's High End Computing Programme. Based on a French initiative, AMMA (http://www.amma-international.org) was built by an international group.

Thanks go to Aaron Boone for providing the ALMIP model data, Malcolm Brooks for providing the NWP forecast data, Francoise Guichard for assistance with the AMMA radiosonde observations and Andreas Fink for help with the interpretation of the radiosonde observations. We would like to thank Le Laboratorie de Météorologie Dynamique for the EPSAT-SG precipitation data and the NOAA National Weather Service Climate Prediction Centre for providing the CMORPH rainfall data. We also acknowledge the TRMM mission scientists

and associated NASA personnel for the production of the TRMM data used in this paper and are grateful to the Goddard Earth Sciences Data and Information Services Center (GES DISC) for making the data available. The GSMaP Project was sponsored by JST-CREST and is promoted by the JAXA Precipitation Measuring Mission (PMM) Science Team, and the GSMaP products were distributed by the Earth Observation Research Center, Japan Aerospace Exploration Agency. Thanks to Nick Dixon for providing Figure 1 and Keith Williams and Caroline Bain for helpful suggestions.

References

Bajamgnigni Gbambie, A. S., and D. G. Steyn (2012), Sea breezes at Cotonou and their interaction with the West African monsoon, *Int. J. Climatol*., doi:10.1002/joc.3637.

Bergès, J, C., F. Chopin, I. Jobard, and R. Roca (2010), EPSAT-SG: A satellite method for precipitation estimation; its concept and implementation for AMMA experiment, *Ann. Geophys*., *28*, 289–308.

Best, M. J., coauthors (2011), The Joint UK Land Environment Simulator (JULES), model description - Part 1: Energy and water fluxes, *Geosci. model Dev., 4*, 677–699.

Biasutti, M., and A. H. Sobel (2009), Delayed Sahel rainfall and global seasonal cycle in a warmer climate, *Geophys. Res. Lett*., ***36***, L23707, doi:10.1029/2009GL041303.

Bielli, S., and R. Roca (2009), Scale decomposition of atmospheric water budget over West Africa during the monsoon 2006 from NCEP/GFS analyses, *Climate Dynamics*, *35*, 143–157.

Bock, O., M.-N. Bouin, A. Walpersdorf, J. P. Lafore, S. Janicot, F. Guichard, and A. Agusti-Panareda (2007), Comparison of ground-based GPS precipitable water vapour to independent observations and numerical weather prediction model re-analyses over Africa, *Quart. J. Roy. Meteor. Soc*., 133, 2011-2027.

Boone, A., I. Poccard-Leclercq, Y. Xue, J. Feng, and P. de Rosnay (2009a), Evaluation of the WAMME model surface fluxes using results from the AMMA land-surface intercomparison project, *Clim. Dyn*., 35, 127-142.

Boone, A., P. de Rosnay, G. Balsamo, A. Beljaars, F. Chopin, B. Decharme, C. Delire, A. Ducharne, S. Gascoin, M. Grippa, F. Guichard, Y. Gusev, P. Harris, L. Jarlan, L. Kergoat, E. Mougin, O. Nasonova, A. Norgaard, T. Orgeval,

C. Ottlé, I. Poccard-Leclercq J. Polcher, I. Sandholt, S. Saux-Picart, C. Taylor, and Y. Xue (2009b), The AMMA land surface model intercomparison project (ALMIP), *Bull. Am. Meteor. Soc., 90*, 1865–1880.

Cieselski, P. E., R. H. Johnson, P. T. Haertal, and J. Wang (2003), Corrected TOGA COARE sounding humidity data: Impact on diagnosed properties of convection and climate over the warm pool, *J. Climate*, *16*, 2370-2384.

Cook, K. H. (2008) The mysteries of Sahel droughts, *Nature Geoscience*, *1*, 647-648.

Dai, A (2006), Precipitation characteristics in eighteen coupled climate models, *J. Climate*. 19, 4605-4630.

Dai, A., X. Lin, and K.-L. Hsu (2007), The frequency, intensity, and diurnal cycle of precipitation in surface and satellite observations over low- and mid-latitudes, *Clim. Dyn*., *29*, 727-744.

Davies, T., M. J. P. Cullen, A. J. Malcolm, M. H. Mawson, A. Staniforth, A. A. White, and S. Wood (2005), A new dynamical core for the Met Office's global and regional modelling of the atmosphere, *Quart. J. Roy. Meteor. Soc., 131*, 1759–1782.

Dirmeyer, P. A., and coauthors (2012), Simulating the diurnal cycle of rainfall in global climate models: Resolution versus parameterisation, *Clim. Dyn., 39*, 399-418.

Duvel, J. P. (1989), Convection over tropical Africa and the Atlantic Ocean during northern summer. Part I: Interannual and diurnal variations, *Mon. Weather Rev*., *117*, 2782-2799.

Essery, R. L. H., M. J. Best, and P. M. Cox (2001), MOSES 2.2 technical documentation. Technical report, Met Office. 14 August 2001.

Garcia-Carreras, L., J. H. Marsham, D. J. Parker, C. L. Bain, S. Milton, A. Saci, M. Salah-Ferroudj, B. Ouchene, and R. Washington (2013), The impact of convective cold pool outflows on model biases in the Sahara, *Geophys. Res. Lett*., 40, 1647–1652..

Geiger, B., C. Meurey, C. Lajas, L. Franchistéguy, D. Carrer, and J.-L. Roujean (2008), Near real-time provision of downwelling shortwave radiation estimates derived from satellite observations, *Meteor. Appl., 15,* 411–420.

Grandpeix, J.-Y., and J.-P. Lafore (2010), A density current parameterization coupled with Emanuel's convection scheme. Part I: The models, *J. Atmos. Sci., 67*, 881–897.

Gregory, D., and P. R. Rowntree (1990), A mass flux convection scheme with representation of cloud ensemble characteristics and stability-dependent closure, *Mon. Wea. Rev., 118*, 1483–1506.

Guichard, F. and coauthors (2004), Modelling the diurnal cycle of deep precipitating convection over land with cloud-resolving models and single-column models, *Q. J. R. Meteorol. Soc*., 130, 3139-3172.

Guichard, F. and coauthors (2010), An intercomparison of simulated rainfall and evapotranspiration associated with a mesoscale convective system over West Africa, *J. Hydrometeorology, 25*, 37–60.

Hagos, S., and C. Zhang (2010), Diabatic heating, divergent circulation and moisture transport in the African monsoon system, *Q. J. R. Meteorol. Soc*., *136*, 411-425.

Holloway, C. E., S. J. Woolnough, and G. M. S. Lister (2012), Precipitation distributions for explicit versus parameterised convection in a large-domain high-resolution tropical case study, *Q. J. R. Meteorol. Soc*., *138*, 1692-1708.

Hoskins, B. (2013), The potential for skill across the range of the seamless weather-climate prediction problem: a stimulus for our science, *Q. J. R. Meteorol. Soc*., *139*, 573-584.

Hourdin, F. and coauthors (2010), AMMA-Model Intercomparison Project, *Bull. Am. Meteorol. Soc*., *91*, 95-104.

Huffman, G. J. and coauthors (2007), The TRMM Multisatellite Precipitation Analysis (TMPA): Quasi-global, multiyear, combined sensor precipitation estimates at fine scales, *J. Hydrometeor*., *8*, 38–55.

Hurrell, J., G. A. Meehl, D. Bader, T. L. Delworth, B. Kirtman, and B. Wielicki (2009), A unified modelling approach to climate system prediction, *Bull. Amer. Meteor. Soc*., *90*, 1891-1832.

Janicot, S., C. D. Thorncroft, A. Ali, N. Asencio, G. Berry, O. Bock, B. Bourles, G. Caniaux, F. Chauvin, A. Deme, L Kergoat, J.-P. Lafore, C. Lavaysse, T. Lebel, B. Marticorena, F. Mounier, P. Nedelec, J. L. Redelsperger, F. Ravegnani, C. E. Reeves, R. Roca, P. de Rosnay, H. Schlager, B. Sultan, M. Tomasini, and A. Ulanovsky (2008),

Large-scale overview of the summer monsoon over West Africa during the AMMA field experiment in 2006, *Ann. Geophys.. 26*, 2569–2595.

Jobard, I., F. Chopin, J. C. Bergès, and R. Roca (2011), An intercomparison of 10-day satellite precipitation products during West African monsoon, *Int. J. Rem. Sens*., *32*, 2353-2376.

Joyce, R., J. E. Janowiak, P. A. Arkin, and P. Xie (2004), CMORPH: A method that produces global precipitation estimates from passive microwave and infrared data at high spatial and temporal resolution, *J. Hydrometeor*., *5*, 487–503.

Lean, H.W., P. A. Clark, M. Dixon, N. M. Roberts, A. Fitch, R. Forbes, and C. Halliwell (2008), Characteristics of high-resolution versions of the Met Office Unified Model for forecasting convection over the United Kingdom, *Mon. Weat. Rev*., *136*, 3408-3424.

Lock, A. P., A. R. Brown, M. R. Bush, G. M. Martin, and R. N. B. Smith (2000), A new boundary layer mixing scheme. Part I: Scheme description and single-column model tests, *Mon. Wea. Rev., 128*, 3187–3199.

Marsham, J.H , N. Dixon, L. Garcia-Carreras. G. M. S. Lister. D. J. Parker. P. Knippertz, and C. Birch, (2013), The role of moist convection in the West African monsoon system – insights from continental-scale convection-permitting simulations, *Geophys. Res. Lett*., 40, 1843-1849.

Masson, V., J.-L. Champeaux, F. Chauvin, C. Meriguet, and R. Lacaze (2003), A global database of land surface parameters at 1-km resolution in meteorological and climate models, *J. Climate, 16,* 1261–1282.

Meynadier, R., O. Bock, F. Guichard, A. Boone, P. Roucou, and J.-L. Redelsperger (2010a), West African Monsoon water cycle: 1. A hybrid water budget data set, *J. Geophys. Res,. 115,* D19106, doi: 10.1029/2010JD013917.

Meynadier, R., O. Bock, S. Gervois, F. Guichard, J.-L. Redelsperger, A. Agusti-Panareda, and A. Beljaars (2010b), West African Monsoon water cycle: 2. Assessment of numerical weather prediction water budgets, *J. Geophys. Res*., *115,* D19107, doi: 10.1029/2010JD013919.

Moncrieff, M., D. Waliser, M. J. Miller, M. A. Shapiro, G. R. Asrar, and J. Caughey (2012), Multiscale convective organisation and the YOTC Virtual Global Field Campaign, *Bull. Amer. Meteor. Soc.,* 93, 1171-1187.

Nesbitt, S. W., and E. J. Zipser (2003), The diurnal cycle of rainfall and convective intensity according to three years of TRMM measurement,. *J. Climate*, *16*, 1456-1475.

Nikulin, G. and coauthors (2012), Precipitation climatology in an ensemble of CORDEX-Africa region climate simulations, *J. Climate*, *25*, 6057-6078.

Nuret, M., J.-P. Lafore, O. Bock, F. Guichard, A. Agusti-Panareda, J.-B. N'Gamini, and J.-L. Redelsperger (2008), Correction of humidity bias for Vaisala RS80-A sondes during the AMMA 2006 observing period, *J. Atmos. Ocean. Tech*., *25*, 2152-2158.

Palmer, T. N., F. J. Doblas-Reyes, A. Weisheimer, and M. J. Rodwell (2008), Toward seamless prediction. Calibration of climate change projections using seasonal forecasts, *Bull. Amer. Meteor. Soc,. 89*, 495-470.

Parker, D. J., R. R. Burton, A. Diongue-Niang, R. J. Ellis, M. Felton, C. M. Taylor, C. D. Thorncroft, P. Bessemoulin, and A. M. Tompkins (2005), The diurnal cycle of the West African Monsoon circulation, *Q. J. R. Meteorol. Soc*., *131*, 2839-2860.

Parker, D. J. and coauthors (2008), The AMMA radiosonde program and its implications for the future of atmospheric monitoring over Africa, *Bull. Amer. Meteor. Soc*., *89*, 1015-1027.

Pearson, K. J., R. J. Hogan, R. P. Allan, G. M. S. Lister, and C. E. Holloway (2010), Evaluation of the model representation of convective systems using satellite observations of outgoing longwave radiation, *J. Geophys. Res*., *115*, D20206, doi:10.1029/2010JD014265.

Pearson, K. J., G. M. S. Lister, C. E. Birch, R. P. Allan, R. J. Hogan, and S. J. Woolnough (2013), Modelling the diurnal cycle of tropical convection across the 'grey zone', *Quart. J. Roy. Meteor. Soc.,* doi:10.1002/qj.2145.

Peixoto, J. P., and A. H. Oort (1983), The atmospheric branch of the hydrological cycle and climate, in *Variations in the Global Weather Budget*, edited by M. Beran and R. Ratcliffe, pp 5-65, D. Reidel, Norwell, Mass.

Pohl, B., and H. Douville (2011), Diagnosing GCM errors over West Africa using relaxation experiments. Part II: Interseasonal variability, *Clim. Dyn*., 37, 1313-1334.

Reynolds, R. W., T. M. Smith, C. Liu, D. B. Chelton, K. S. Casey, and M. G. Schlax (2007), Daily high-resolution blended analyses for sea surface temperature*, J. Climate*, *20*, 5473-5496.

Rio, C., F. Hourdin, J.-Y. Grandpeix, and J.-P. Lafore (2009), Shifting the diurnal cycle of parameterized deep convection over land, *Geophys. Res. Lett., 36*, L07809, DOI: 10.1029/2008GL036779.

Roca, R., P. Chambon, I. Jobard, P.-E.Kirstetter, M. Gosset and J. C. Bergès (2010), Comparing satellite and surface rainfall products over West Africa at meteorologically relevant scales during the AMMA campaign using error estimates, *J. App. Meteorol. Climatol., 49*, 715-731.

Sane, Y (2012) An analysis of the diurnal cycle of precipitation over Dakar using local rain-gauge data and a general circulation model, *Q. J. Meteorol. Soc*., *138*, 2182-2195.

Stephens, G. L. and coauthors (2010), Dreary state of precipitation in global models, *J. Geophys. Res. Atmos*., *115,* DOI: 10.1029/2010JD014532.

Stirling, A. J., and R. A. Stratton (2012), Entrainment processes in the diurnal cycle of deep convection over land, *Q. J. Meteorol. Soc*., *138*, 1135-1149.

Stratton, R. A., and A. J. Stirling (2012), Improving the diurnal cycle of convection in GCMs, *Q. J. Meteorol. Soc*., 138, 1121-1134.

Tompkins, A. M., A. Diongue-Niang, D. J. Parker, and C. D. Thorncroft (2005) The African easterly jet in the ECMWF Integrated Forecast System: 4D-Var analysis, *Q. J. Meteorol. Soc*., *131*, 2861-2885.

Ushio, T., K. Sasashige, T. Kubota, S. Shige, K. Okamoto, K. Aonashi, T. Inoue, N. Takahashi, T. Iguchi, M. Kachi, R. Oki, T. Morimoto, and Z. Kawasaki (2009), A Kalman filter approach to the Global Satellite Mapping of Precipitation (GSMaP) from combined passive microwave and infrared radiometric data, *J. Meteorol. Soc. Jap*., 87, 137–151.

Waliser, D, and coauthors (2012) The “Year” of Tropical Convection (May 2008–April 2010): Climate Variability and Weather Highlights, *Bull. Amer. Meteor. Soc.*, *93*, 1189–1218.

Walters, D. N., M. J. Best, A. C. Bushell, D. Copsey, J. M. Edwards, P. D. Falloon, C. M. Harris, A. P. Lock, J. C. Manners, C. J. Morcrette, M. J. Roberts, R. A. Stratton, S. Webster, J. M. Wilkinson, M. R. Willett, I. A. Boutle, P. D. Earnshaw, P. G. Hill, C. MacLachlan, G. M. Martin, W. Moufouma-Okia, M. D. Palmer, J. C. Petch, G. G. Rooney, A. A. Scaife, and K. D. Williams (2011), The Met Office Unified Model Global Atmosphere 3.0/3.1 and JULES Global Land 3.0/3.1 configurations, *Geosci. Model Dev.,* 4, 919-941.

Weisman, M. L., W. C. Skamarock, and J. B. Klemp (1997), The resolution dependence of explicitly modeled convective systems, *Mon. Wea. Rev., 125*, 527–548.

Wilson, D. R., and S. P. Ballard (1999), A microphysically based precipitation scheme for the U.K. Meteorological Office Unified Model, *Quart. J. Roy. Meteor. Soc., 125*, 1607–1636.

Yang, G.-Y., and J. Slingo J (2001) The diurnal cycle in the tropics, *Mon. Weat. Rev*., *129*, 784-801.

Table 1 Summary of the model simulations

Simulation	Convection	Vertical levels	Run length	LBC's from	Referred to as
1.5 km	Explicit	70	9 days	4kmExp nest	1.5kmExp
4 km	Explicit	70	40 days	12kmParam nest	4kmExp
12 km	Explicit	38	40 days	ECMWF analyses	12kmExp
12 km	Parameterised	38	40 days	ECMWF analyses	12kmParam
40 km	Parameterised	38	40 days	ECMWF analyses	40kmParam
NWP analyses	Parameterised	38	40 days	N/A	Analyses
Climate	Parameterised	85	10 years	N/A	Climate

.

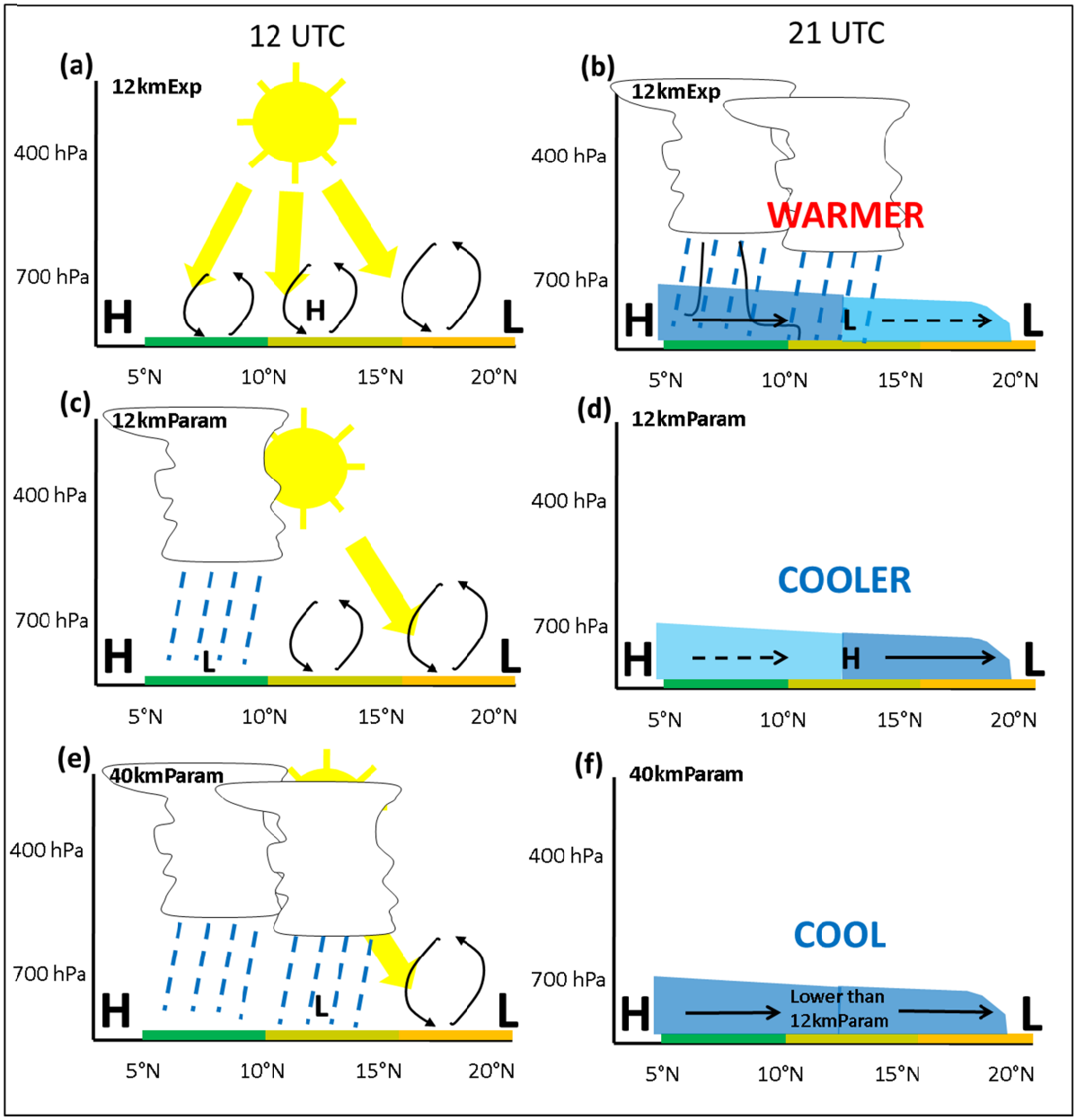

Figure 1 Schematic illustrating the conclusions of *Marsham et al.* [2013] and the impact on the water budget. These models are archetypes of typical model behaviour with parameterised and explicitly-resolved convection.

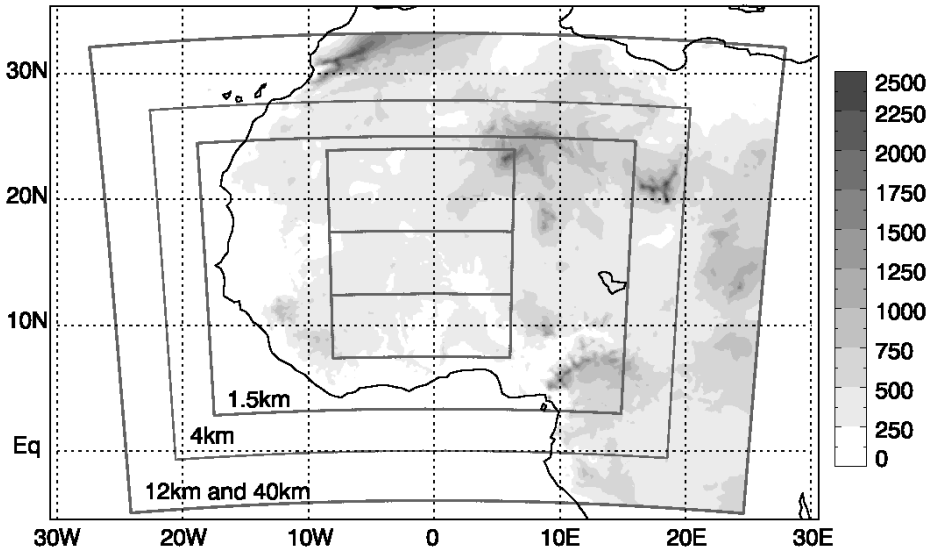

Figure 2 Orography height and limited area model domain boundaries. The upper (17.5-24°N, 8°W-6°E), mid (12.5-17.5°N, 8°W-6°E) and lower (7.5-12.5°N, 8°W-6°E) boxes are used for averaging in Figures 11-14. Data are averaged over all three of these boxes (7.5-24°N, 8°W-6°E) in Figure 3.

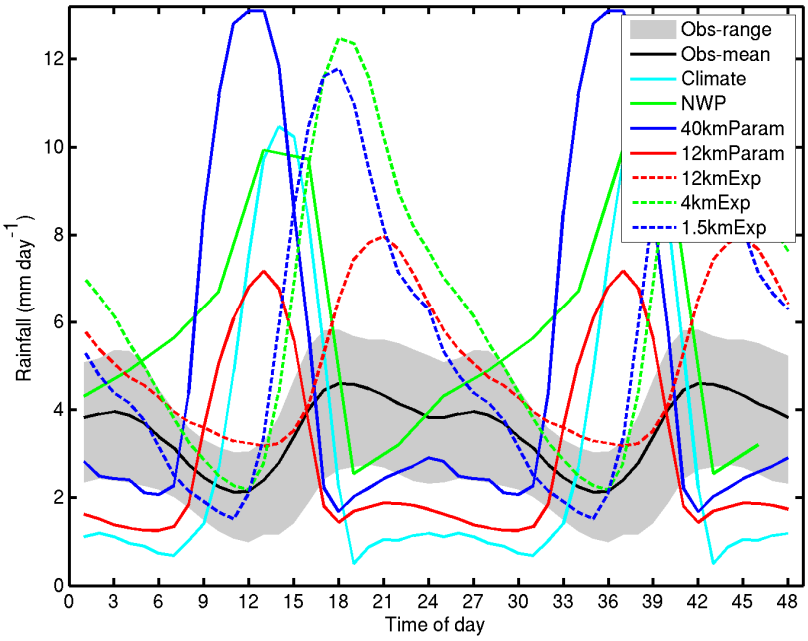

Figure 3 Mean diurnal cycle of rainfall. The grey area represents the range (minimum and maximum) of the satellite products.

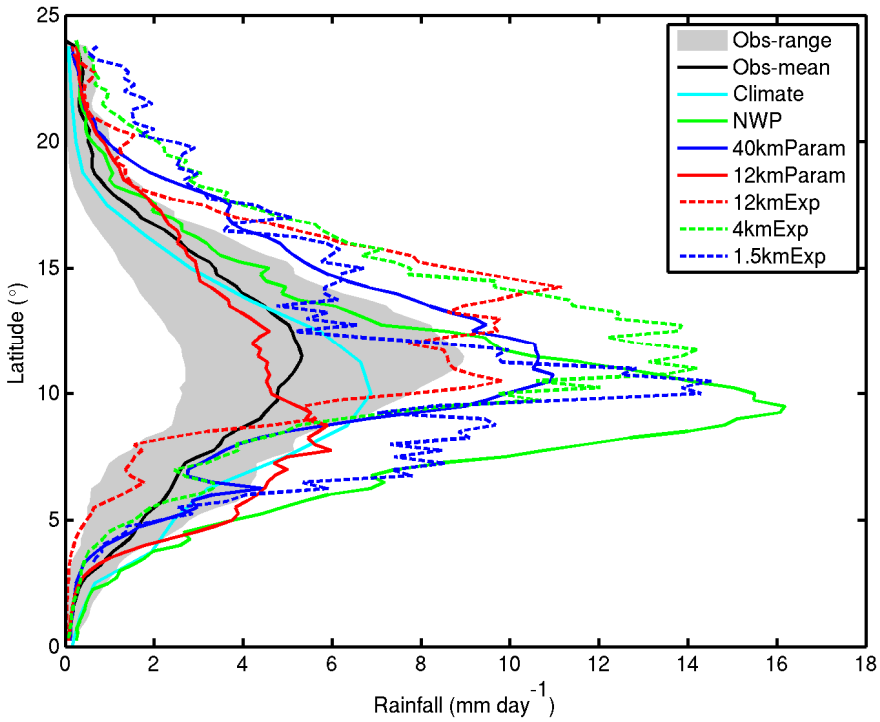

Figure 4 Mean rainfall by latitude, averaged 8°W-6°E. Data from 4kmExp and 1.5kmExp are smoothed to 12 km resolution. The grey area represents the range (minimum and maximum) of the satellite products.

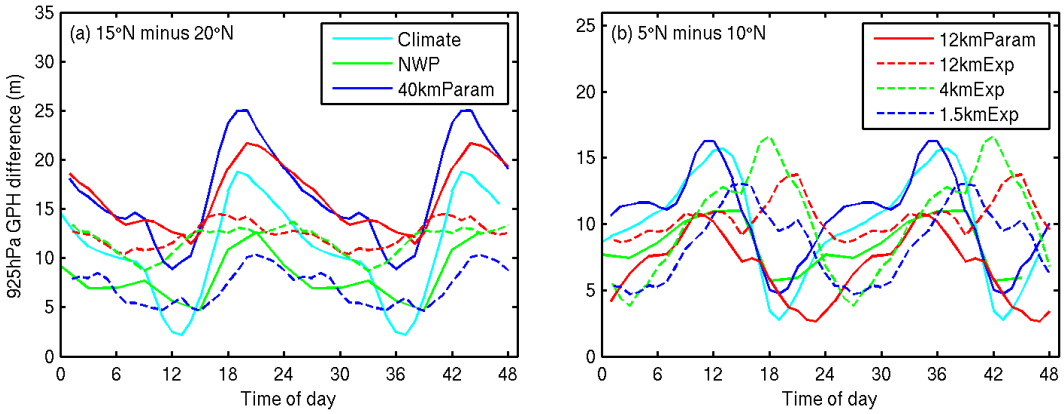

Figure 5 Mean diurnal cycle of the difference in 925hPa geopotential height averaged over 8°W-6°E and between (a) 15 and 20°N and between (b) 5 and 10°N.

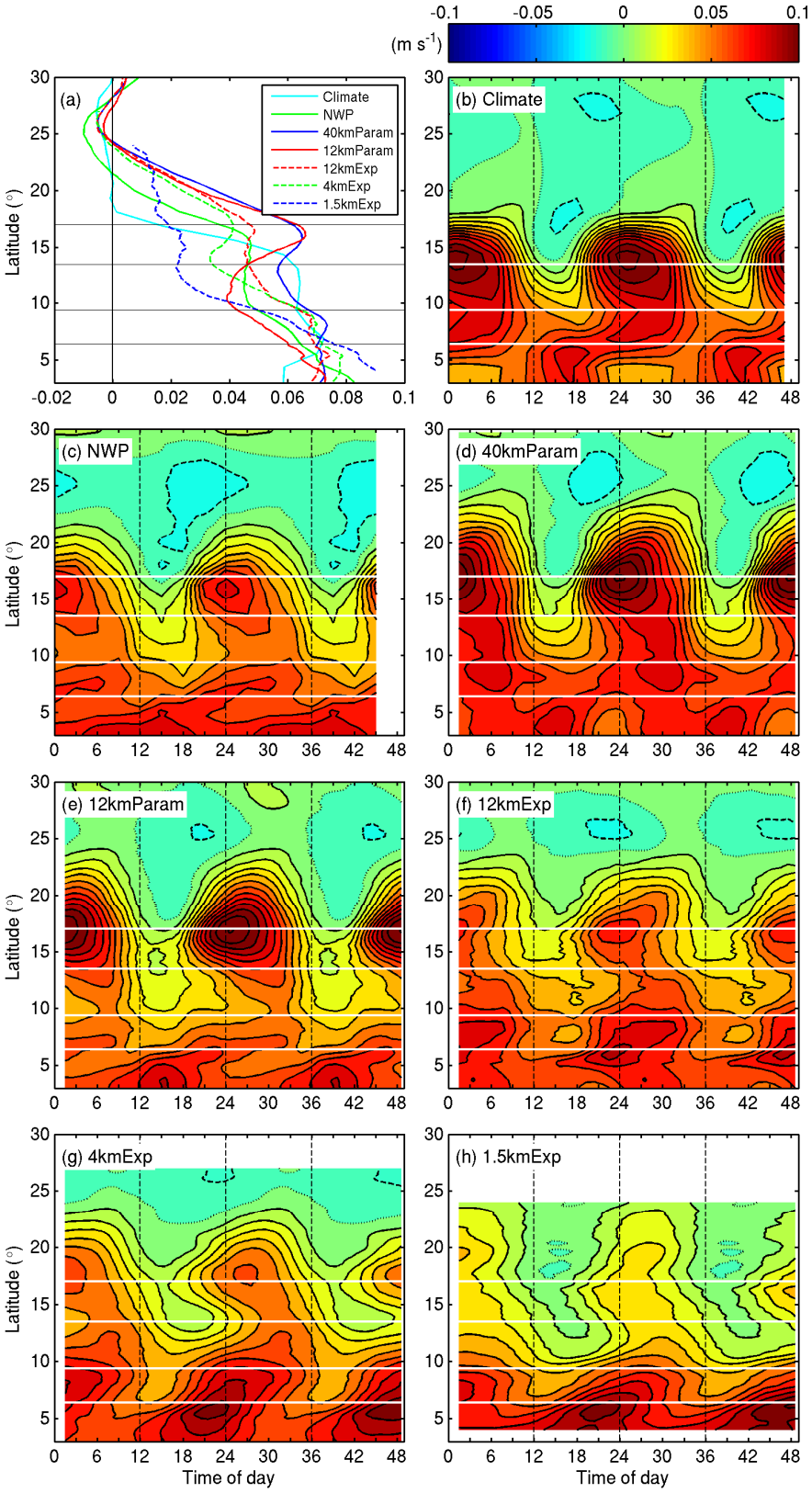

Figure 6 Moisture advection (v*q) for each of the models at 400 m agl averaged between 8°W and 6°E. Diagnostics from the 4 and 1.5 km domains are smoothed to 12 km resolution. The horizontal white lines mark the latitude of the four radiosonde stations used in Figure 7.

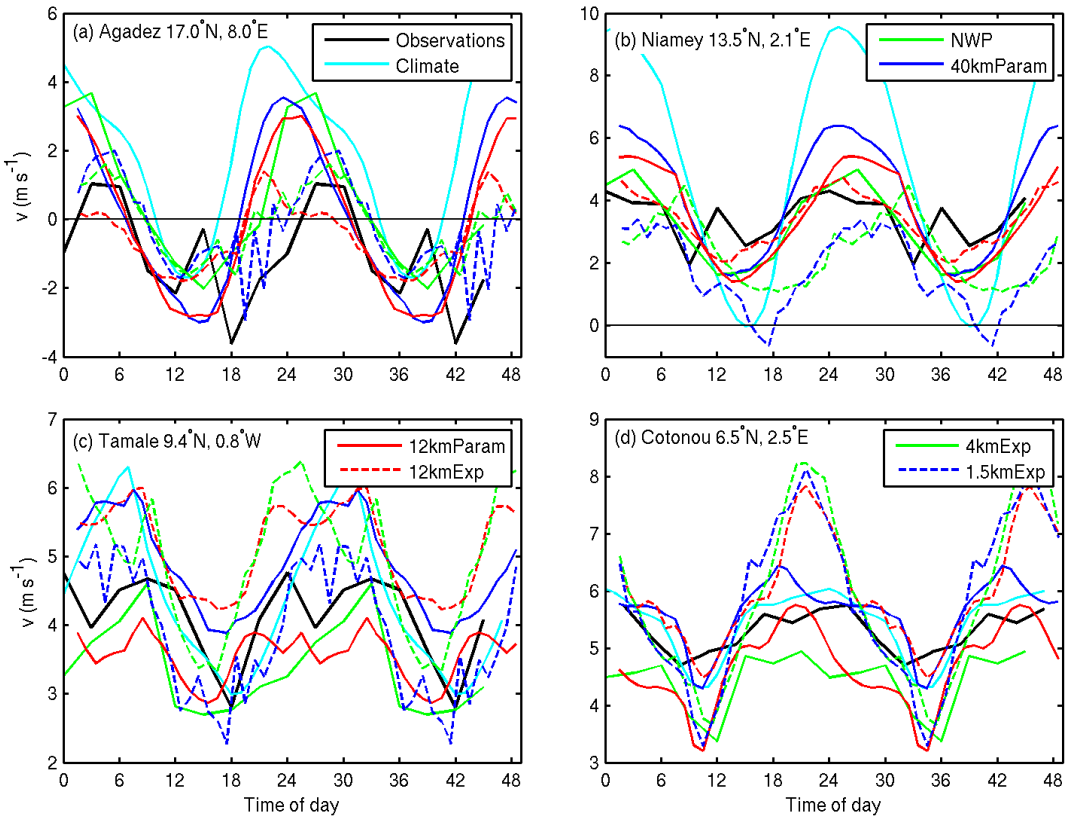

Figure 7 Mean diurnal cycle in meridional wind speeds, *v*, at 400 m agl from the models and observations. Note that the data for the climate model in panel (a) was taken from 13.5°N, 8.0°E to allow for the fact that the entire monsoon system is too far south in this model.

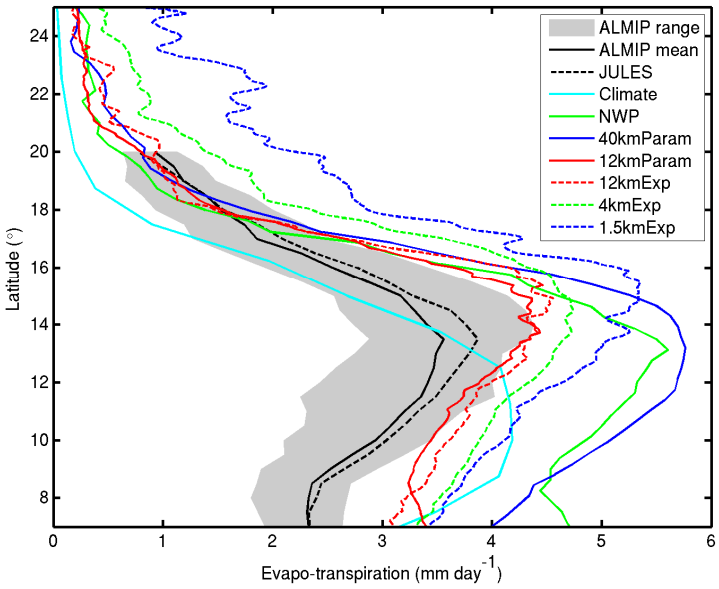

Figure 8 Mean latitude plot of evapotranspiration averaged between 8°W and 6°E. The data from 4kmExp and 1.5kmExp are smoothed to 12 km resolution. The grey area represents the range (minimum and maximum) of the ALMIP simulations.

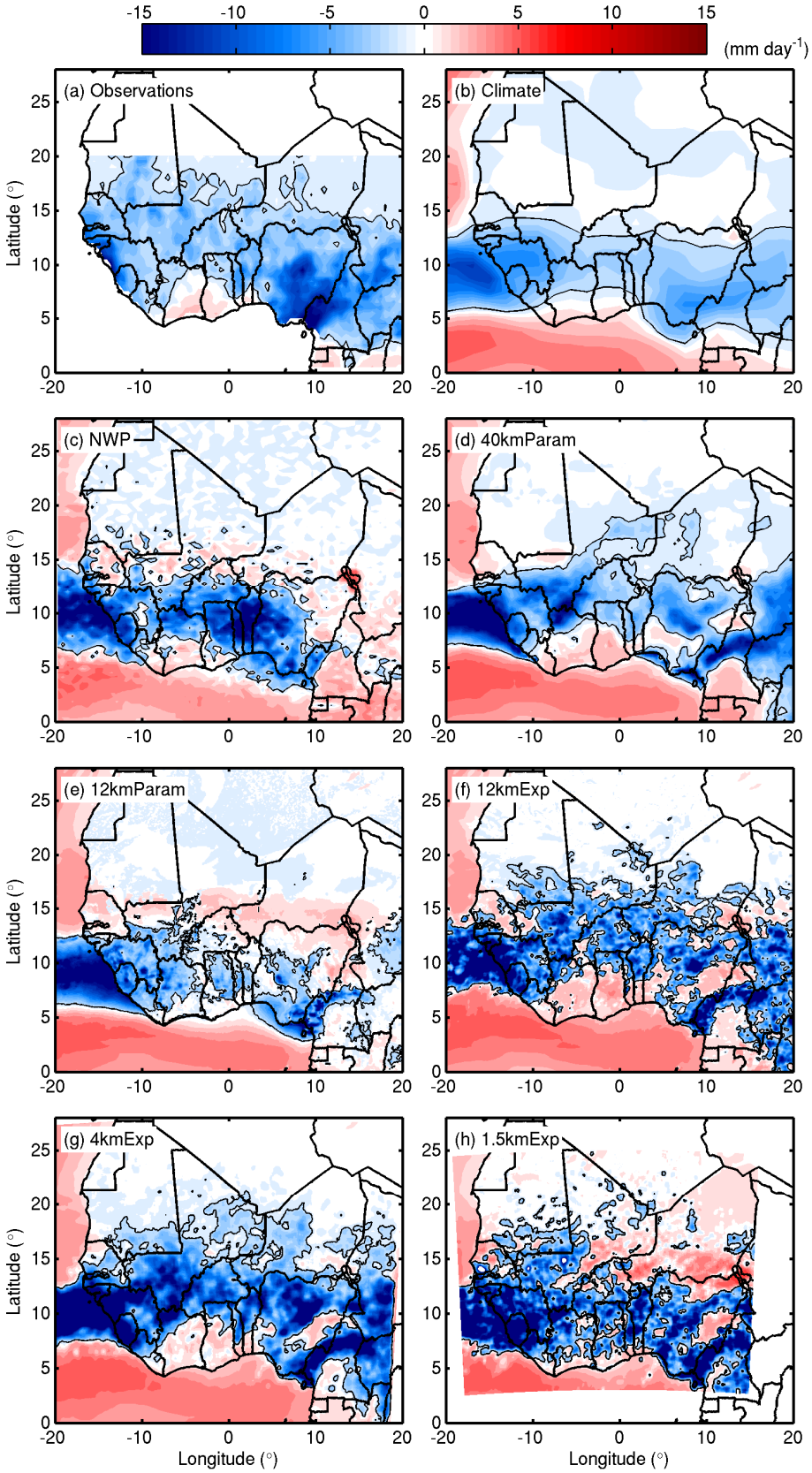

Figure 9 40-day mean *E* minus *P*. The black contour is at -1 mm day^{-1}.

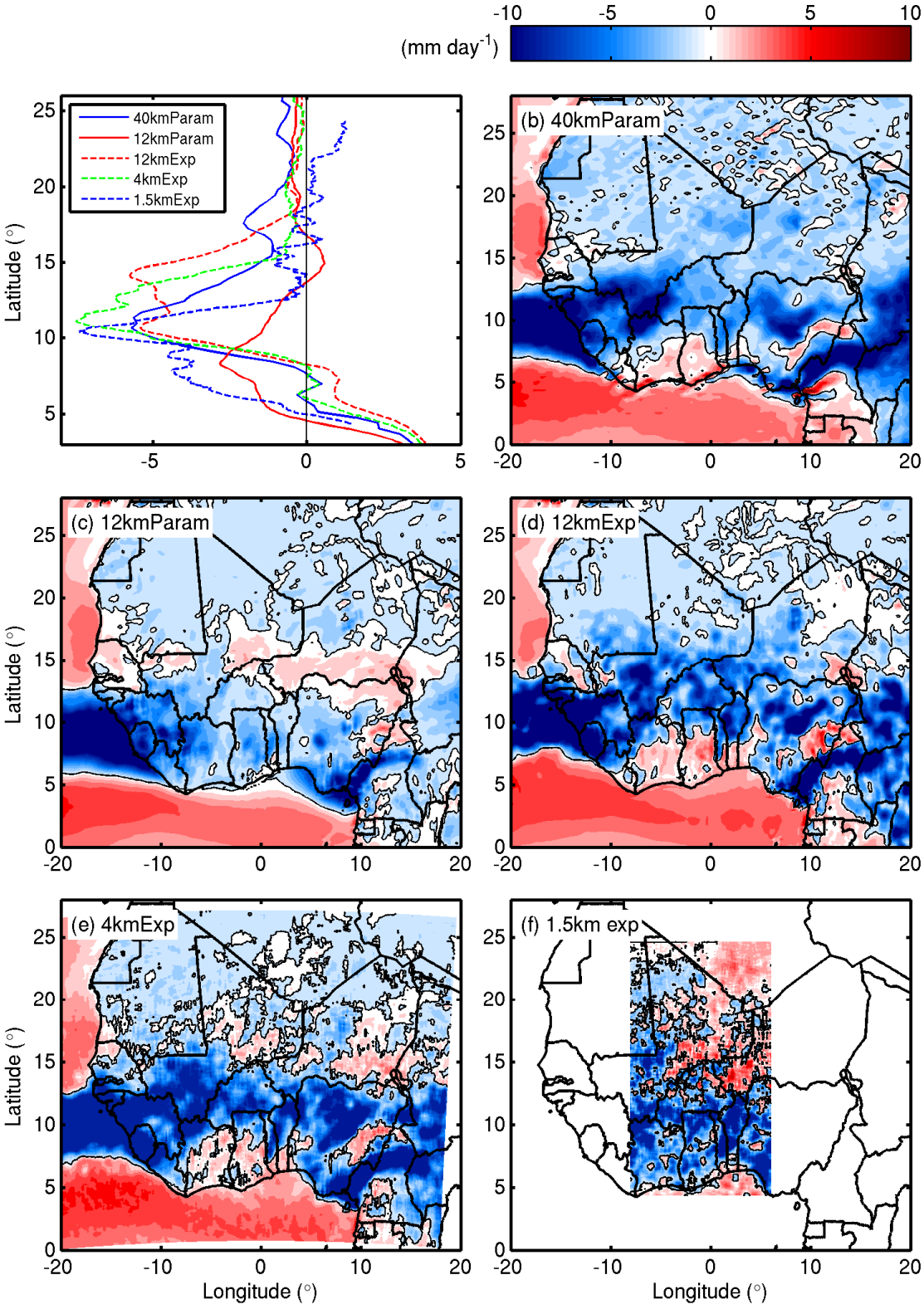

Figure 10 40-day mean MFD integrated over whole atmospheric column. (a) is averaged between 8°W and 6°E and the x-axis is MFD (mm day^{-1}). The black contour is at -1 mm day^{-1}. Due to computational limitations MFD was only computed for 1.5kmExp within the analyses boxes marked in Figure 1 (7.5-24°N, 8°W-6°E).

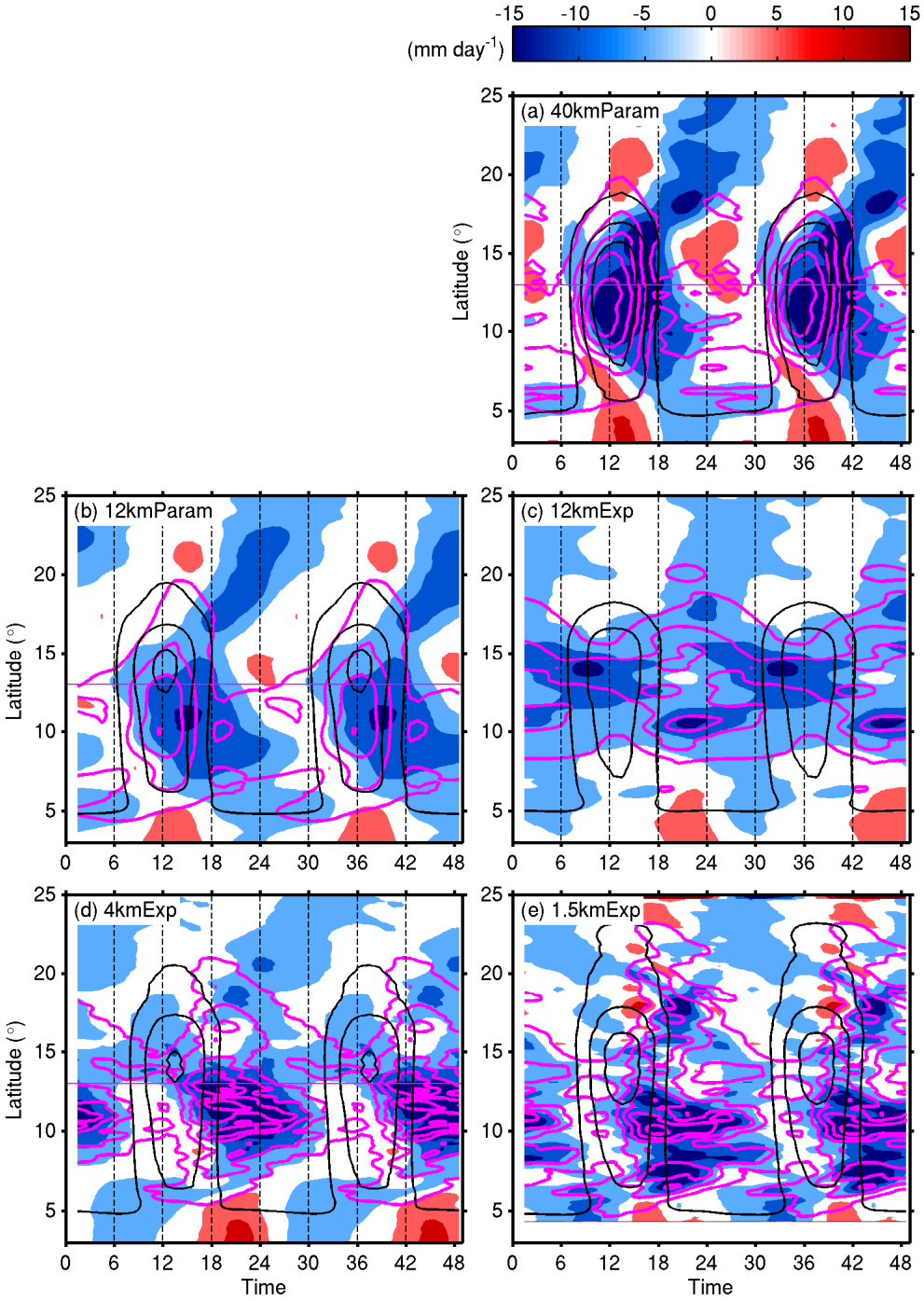

Figure 11 Mean diurnal cycle of MFD (shading), precipitation (pink contours) and evaptranspiration (black contours), averaged between -8 and 6°E.

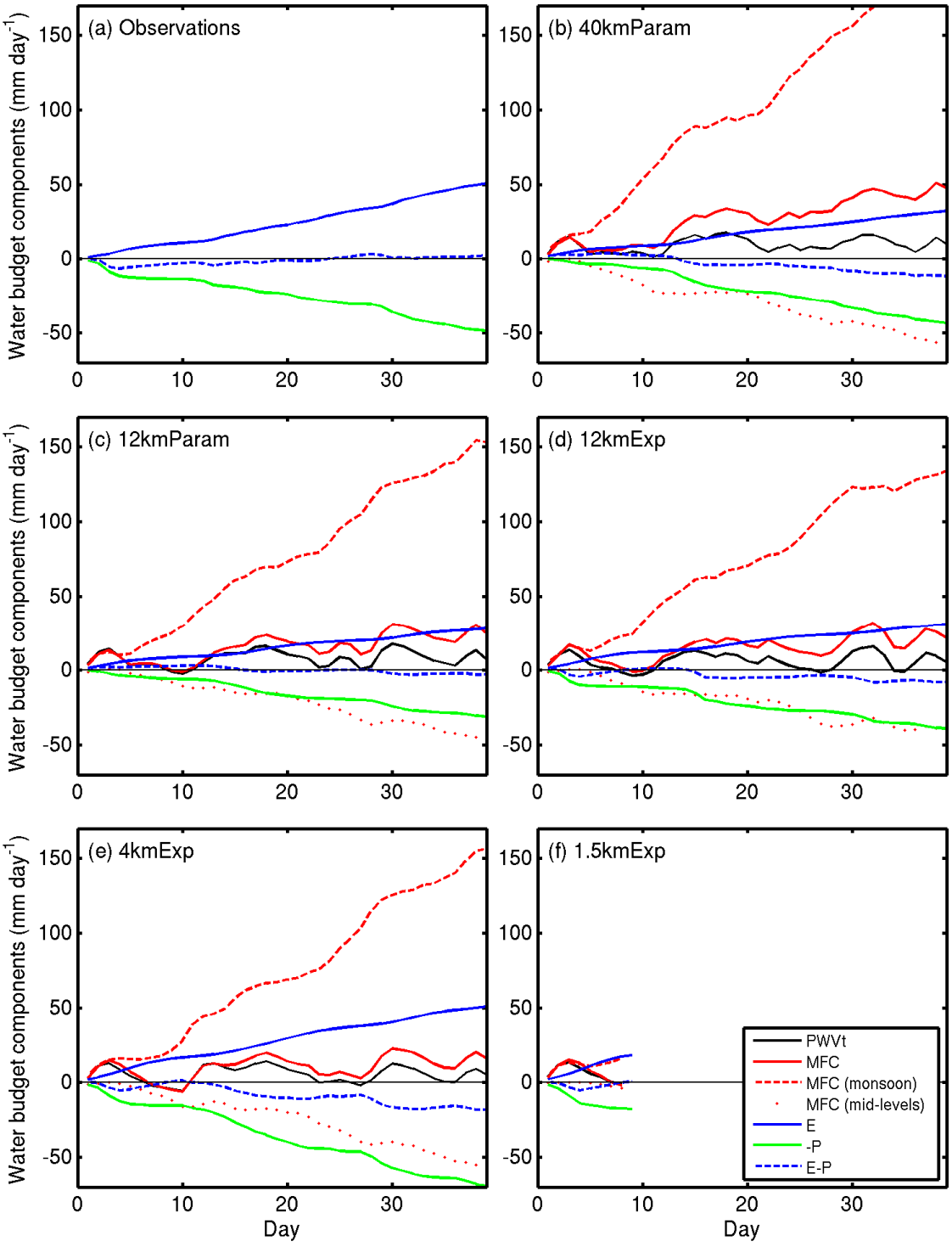

Figure 12 Cumulative plots of the terms of the water budget in the northern box (17.5-24°N).

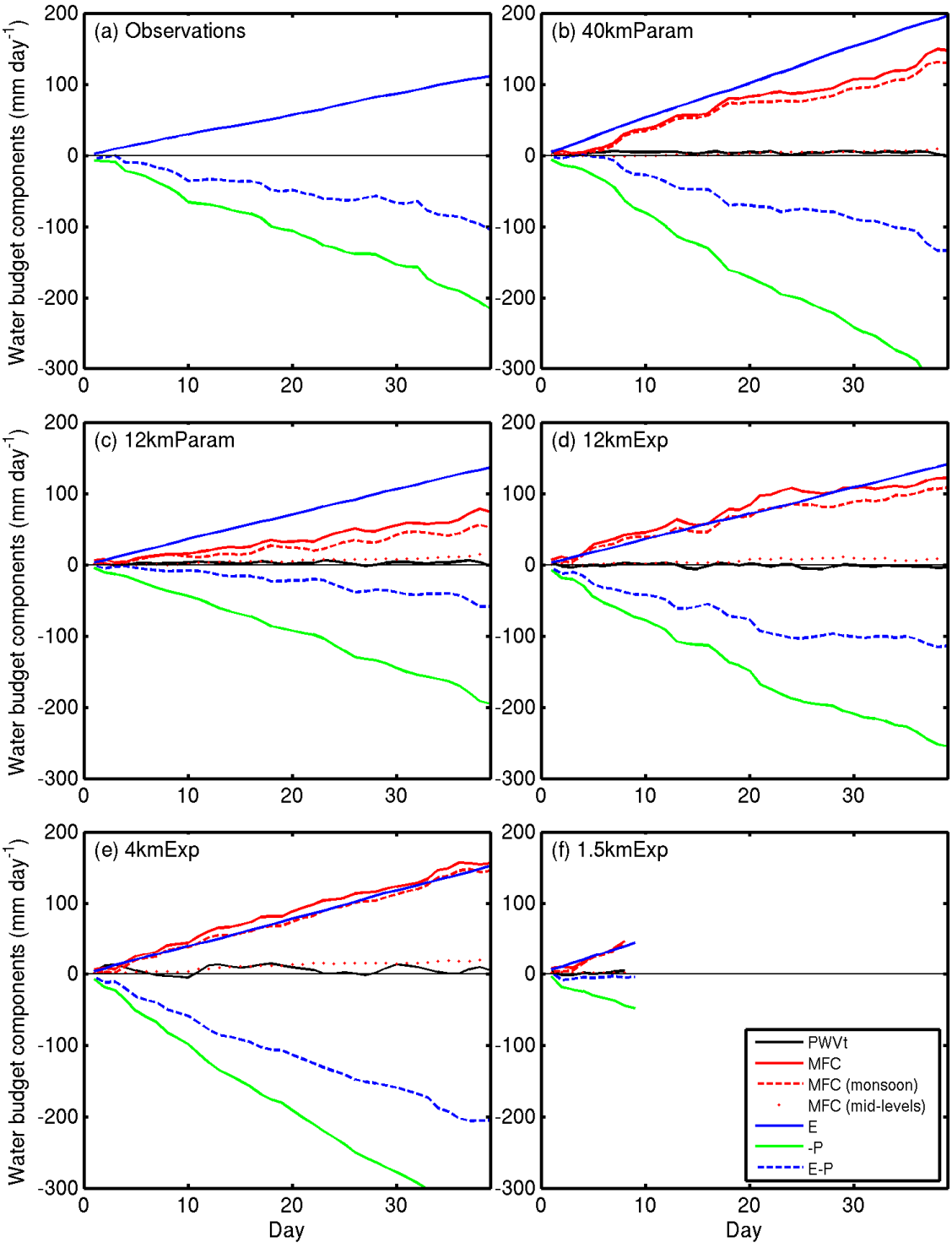

Figure 13 Cumulative plots of the terms of the water budget in the southern box (7.5-12.5N).

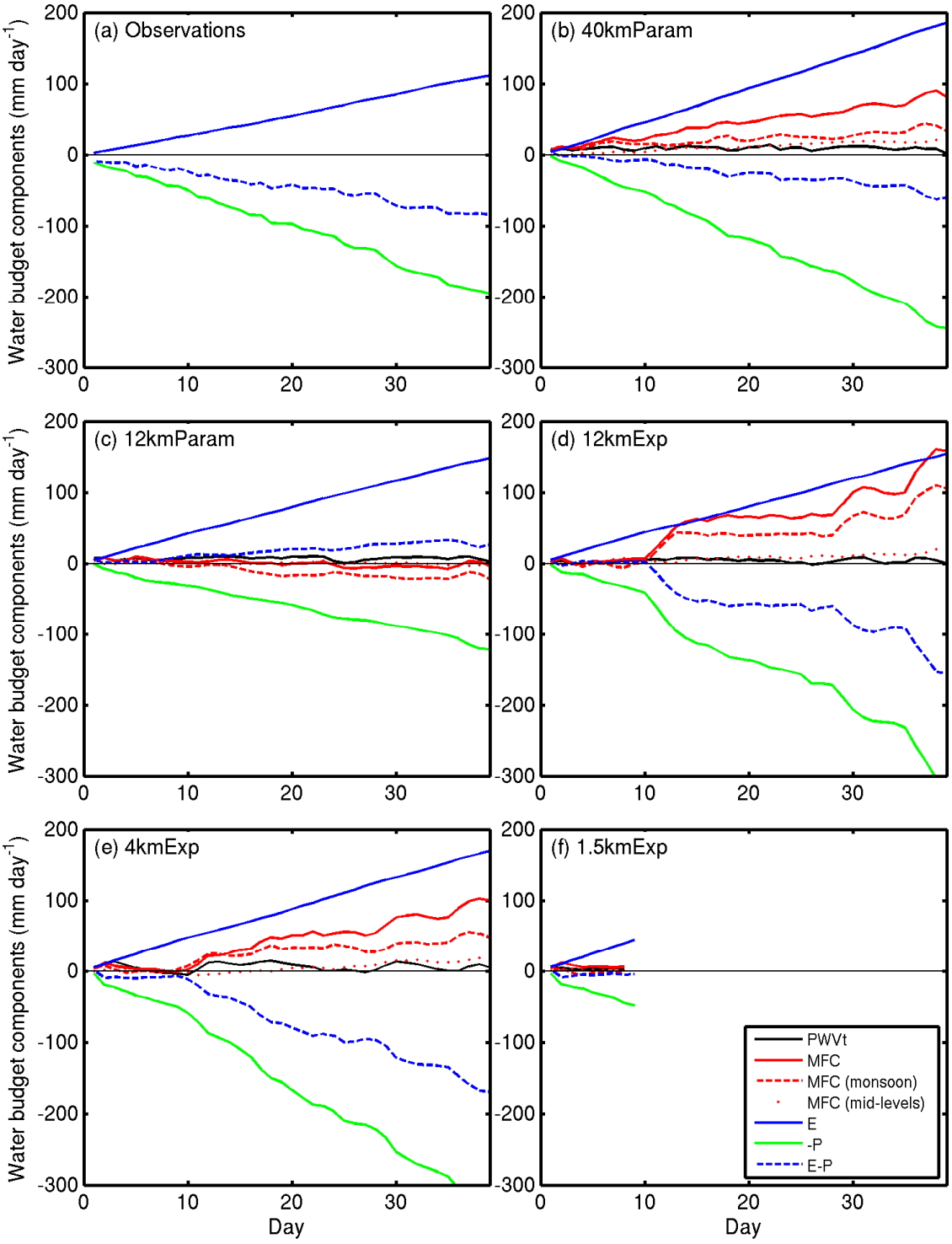

Figure 14 Cumulative plots of the terms of the water budget in the mid box (12.5-17.5°N).